

**Control of spiral wave dynamics
by feedback mechanism via
a triangular sensory domain**

Dissertation

zur Erlangung des akademischen Grades

**doctor rerum naturalium
(Dr.rer.nat.)**

genehmigt durch die Fakultät für Naturwissenschaften
der Otto-von-Guericke-Universität Magdeburg

von **M.Sc. Somprasong Naknaimueang**

geb. am **24.Mai 1973** in **Nakhonratchasima**

Gutachter: PD Dr. Marcus J.B Hauser
Prof. Dr. Katharina Krischer

eingereicht am: 30. Mai 2006

verteidigt am: 14. November 2006

Acknowledgements

I would like to first acknowledge my supervisor Prof. Stefan C. Müller for giving me a great opportunity to work in this group. I am also very grateful to his support and kindness. I am also grateful to Dr. Marcus Hauser who gave me a very helpful advice and always help me to find the solution of the problems in many things and being approachable. Also many thanks go to Dr. Thomas Mair for his companionship, his advice and giving me great encouragement about this work. I am greatly indebted to the very good colleagues and friends who always spent their time to listen my problems and always cheer me up: Dr. Wolfgang Jantoss, Frau Uta Lehmann, Frau Erika Matthies, Frau Vera Neumann, Christian Warnke and Frank Rietz.

I would also like to take this opportunity to thank Iris Cassidy for her worth friendship, support and big help in all things over the years. I am appreciate to Lenka Sebestíková my flatmate who never mind in small things and cooked sometime for me very delicious food. The support from all group that I should never forget to acknowledge; Uli Storb, Jan Tusch, Ronny Straube, Katja Gutmann and Ramona Bengsch. My thanks word also go to Dr. On-Uma Kheowan who provided and gave me an important hint to start this work.

Special thanks go to Christiane Hilgardt who always be with me to cheer me up and wipe away the tears and stand by me when I have a bad day. Also great thanks to Elena Slámová who was always with me and gave me a lecture how to behave and how to think in positive way. My heartfelt appreciation to Nico Fricke and Olaf Karopka who gave me a precious friendship that more than word I can say. My deeply heartily truly thanks to Dr. Michael Antony Allen, Physics Department, Faculty of Science, Mahidol University who gave me a great encouragement, a big support, a very helpful advice and very useful suggestions about the whole work. And I will never go throughout all those days without supporting (in memory) from my sweetheart mother.

Finally I would like to thank the Graduiertenförderung and Neuroverbund Sachsen-Anhalt for financial support.

Somprasong Naknaimueang

Contents

1	Introduction	9
1.1	Travelling waves	10
1.2	Excitable systems	15
1.3	Motion of the spiral tip	19
1.4	Spiral wave dynamics under feedback control	21
1.5	The light-sensitive Belousov-Zhabotinsky reaction	27
1.6	Outline	29
2	Experimental Part	31
2.1	Preparation of chemicals	31
2.2	Generation of a single spiral wave	34
2.3	Experimental setup	36
2.4	Controlling program	37
2.5	Obtaining the control parameters	40
2.6	Image analysis	41
3	Numerical Calculation	42
3.1	Numerical solution of excitable system equations	42
3.2	Drift vector field	44
3.3	Divergence plot	46
4	Plane Wave Approximation	49
5	Experimental and Numerical Results	52
5.1	Equilateral triangular domain	52
5.2	Isosceles triangular domain	67
5.3	Discussion	72
6	Conclusion	74

Summary

Experimental and computational examinations of the trajectories of spiral wave cores were performed in excitable systems whose excitability is modulated in proportion to the integral of the activity in a sensory domain. The experimental observations were carried out using the light-sensitive Belousov-Zhabotinsky (BZ) reaction. The light-sensitive catalyst was $\text{Ru}(\text{bpy})_3^{2+}$. For this reaction an increase in light results in a decrease in excitability. The numerical work was performed using a generic piecewise-linear excitable system model.

The sensory domains used were in the shape of either equilateral or isosceles triangles. The behaviour of the spiral core was determined as a function of the domain size and the ratio of the base length and height of the triangle. These types of domain exhibit a distinctly different series of bifurcations as compared with other domain geometries studied so far on account of this domain shape having vertices opposite sides. In particular, novel forms of lobed limit cycles occur which are destroyed and then re-form as the domain size is varied.

We also introduce the concept of express and stagnation zones which are regions where the trajectory moves particularly rapidly or slowly, respectively. Although these regions can be very prominent for triangular domains, they also occur for other domain geometries such as squares. They are of interest in the manipulation of spiral waves since, like stable fixed points, stagnation zones are to be avoided if the spiral wave is to be moved rapidly from one place to another.

To give a global picture of the behaviour of the spiral core for a particular domain, a vector plot indicating the spiral core drift velocity on a lattice of points in and around the domain is generally used. Such plots can be rather complicated and to facilitate their interpretation we have developed a colour-

coding scheme for the arrows and the background based on the normalized divergence of the vector field at each point. This makes it easier to distinguish between attracting and repelling limit cycles and makes stagnation zones particularly prominent.

Finally, we have formulated a simple method which is referred to as the plane wave approximation (PWA) that can be used to account for some of the behaviour seen far from the sensory domain. In this approach, the parts of the spiral wave crossing the sensory domain are treated as a series of plane waves. The PWA allows one to determine the directions in which express and stagnation zones lie far from the domain, and also account for how prominent these zones are. The limit cycles that the spiral core tends to are sometimes composed partly of attracting express zones. The PWA can also be used to find the distances of these regions from the domain.

Zusammenfassung

Gegenstand der vorliegenden Dissertation ist die Untersuchung der Steuerung von selbstorganisierten Raum-Zeit-Strukturen in einem chemischen System. Als Untersuchungsgegenstand wird die Belousov-Zhabotinsky-Reaktion verwendet, die, ein sowohl experimentell als auch theoretisch gut erforschtes Modellsystem zur Analyse der Strukturbildung in erregbaren Medien darstellt. Bei dieser Reaktion können aufgrund der nichtlinearen Dynamik der Reaktionsprozesse in Verbindung mit Diffusion eine Vielzahl von Erregungsmustern auftreten. Propagierende Erregungswellen sind in ein-, zwei- und dreidimensionalen Systemen beobachtet worden. Im Rahmen der Arbeit sind dabei spiralförmige Erregungswellen von Interesse, die mittels Rückkopplung kontrolliert werden. Das Verständnis der komplexen Dynamik solcher modulierten Spiralwellen ist eine Grundvoraussetzung für die Entwicklung von Methoden zur Kontrolle dieser Spiralwellen, die in biologischen Systemen eine hohe Anwendungsrelevanz (Spiralwellen auf dem Herzmuskelgewebe) besitzen.

Die vorliegende Arbeit untersucht die Trajektorien von Spiralwellenkernen in erregbaren Systemen, wobei die Erregbarkeit des gesamten Systems (globale Rückkopplung) in Abhängigkeit von der Aktivität eines festgelegten Raumbereiches (sensorische Domäne) moduliert wird. Um dies zu erreichen wurden die Experimente mit der lichtempfindlichen BZ-Reaktion durchgeführt, bei der die Lichtempfindlichkeit des Katalysators Ru_3^{2+} genutzt wird. Ru_3^{2+} wirkt in der Reaktion als Inhibitor und somit kann über die Lichtintensität die Erregbarkeit des Systems reguliert werden. Eine Erhöhung der Lichtintensität bewirkt dabei eine Abnahme der Erregbarkeit. Parallel zu den Experimenten wurden die Ergebnisse mit numerischen Simulationen der entsprechenden Reaktions-Diffusionsgleichungen verglichen.

Als geometrische Form der sensorischen Domäne sind gleichseitige und gle-

ichschenklige Dreiecke verwendet worden. Das Verhalten des Spiralwellenkerns wurde zum einen als Funktion der Domänengröße und zum anderen in Abhängigkeit vom Verhältnis der Basislänge zur Höhe des Dreiecks bestimmt. Die verwendeten Geometrietypen der Domäne ergeben eine Bifurkationsserie, die im Vergleich zu den bisher untersuchten Domänengeometrien (Kreise, Ellipsen, Quadrate, Rechtecke) große Unterschiede aufweist. Die Ursache liegt darin, dass jedem Eckpunkt des Dreiecks eine Seite gegenüberliegt. Insbesondere treten neuartige Formen von Grenzyklen auf, die durch Variation der Domänengröße zerstört und dann neu ausgebildet werden können.

Es wurde das Konzept von Beschleunigungs- und Stagnationszonen eingeführt. Das sind Bereiche in denen sich die Trajektorien sehr schnell beziehungsweise sehr langsam bewegen. In den Stagnationszonen kann es sogar dazu kommen, dass die Spiralkerne an einem Punkt verharren, das heißt es befinden sich dort stabile Fixpunkte. Für die dreieckigen Domänen erweisen sich die Beschleunigungs- und Stagnationszonen von großer Bedeutung, sie sind dort stärker ausgeprägt als in den anderen Domänengeometrien in denen sie vorkommen (Quadrate). Diese Zonen sind bei der Manipulation von Spiralwellen von Interesse, denn wenn eine Spiralwelle mit hoher Geschwindigkeit von einem Ort zum anderen bewegt werden soll, erweisen sich stabile Fixpunkte und Stagnationszonen als Hindernis.

Um eine Übersicht über das Verhalten von Spiralkernen für eine spezielle Domäne zu geben, wurde ein Vektorfeld berechnet, das die Geschwindigkeit der Spiralkerndrift auf einem Gitter der Domäne sowie ihrer unmittelbaren Umgebung darstellt. Solche Vektorfelder können unter Umständen sehr kompliziert und somit auch schwer zu deuten sein. Zur Interpretationserleichterung wurde eine Farbcodierung entwickelt, die auf der normalisierten Divergenz des Vektorfeldes für jeden Punkt basiert. Dieses Programm erleichtert die Unterscheidung zwischen anziehenden und abstoßenden Grenzyklen und hebt die Stagnationszonen deutlich hervor.

Desweiteren wurde eine einfache Methode entwickelt, welche wir als Plane wave approximation (PWA) bezeichnen, die zur Charakterisierung der Spiralkerndrift fern der Domäne dient. Diese Methode kann für beliebige Domänengeometrien benutzt werden. Dabei wird angenommen, dass die Teile der Spiralwelle, welche die Domäne durchkreuzen eine Serie von ebenen Wellen

bildet. Die PWA ermöglicht es dann die Richtungen zu bestimmen, in der Beschleunigungs- und Stagnationszonen fern der Domäne liegen. Außerdem kann die Stärke des Einflusses dieser Zonen auf die Bewegung des Spiralkerns bestimmt werden. Die Grenzyklen, auf dem sich der Spiralkern bewegt, setzen sich manchmal (teilweise) aus anziehenden Beschleunigungszonen zusammen. Die PWA ist weiterhin in der Lage den Abstand dieser Bereiche zur Domäne anzugeben.

Chapter 1

Introduction

This thesis is concerned with a certain type of pattern formation and its subsequent manipulation. Pattern formation is the spontaneous appearance of a non-uniform distribution which is referred to as a ‘pattern.’ Patterns appear in a wide variety of systems such as fingerprints, stripes of a tiger or zebra [1], spots of a leopard [2], galaxies and stars [3], nerve conduction [4], heart muscle [5] and aggregating slime-mould cells [6] as illustrated in Fig. 1.1.

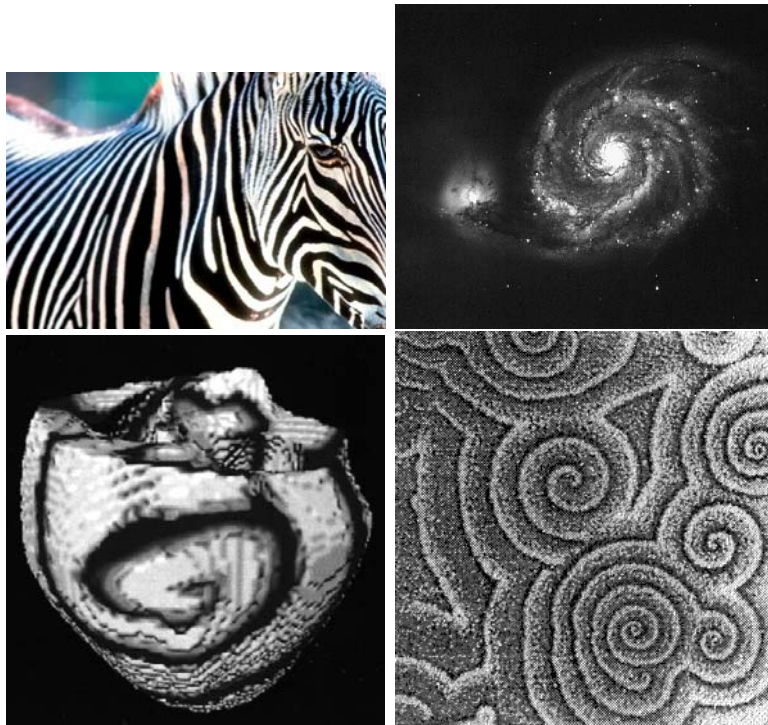


Figure 1.1: Examples of pattern formation in nature. From [7]

Pattern formation occurs as the result of the uniform (unpatterned) state becoming unstable when the system is driven away from its stable uniform state by a large disturbance. The patterns can be either stationary like in animal coats or moving like the rotating spiral waves we will be considering. In both cases the system is nonlinear and needs to be maintained far from equilibrium. The patterns result from the interplay between local dynamical processes and diffusive transport.

The most important example of stationary pattern formation is the Turing mechanism [8]. Alan Turing proposed a simple reaction-diffusion system describing chemical reactions and diffusion to account for morphogenesis, i.e., the development of form and shape in biological systems..

Both Turing patterns and the non-stationary patterns we will be studying occur in reaction-diffusion systems. These are governed by equations of the form

$$\frac{\partial \mathbf{u}}{\partial t} = \mathcal{D} \nabla^2 \mathbf{u} + \mathbf{f}(\mathbf{u}) \quad (1.1)$$

in which the dependent variables \mathbf{u} and the reaction terms $\mathbf{f}(\mathbf{u})$ are vectors of quantities and \mathcal{D} is a diagonal matrix of diffusion coefficients.

1.1 Travelling waves

The simplest type of non-stationary patterns take the form of travelling waves. Such waves can be periodic or non-periodic. In one dimension, non-periodic waves can take the form of either pulses or kinks. As illustrated in Fig. 1.2, pulses leave the state of the system unchanged after they have passed. With kinks, the state of the system ahead of the wavefront is different from the state behind the wavefront.

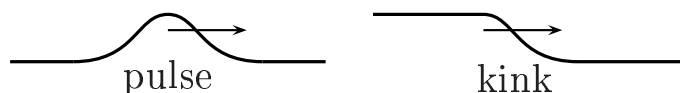


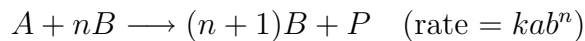
Figure 1.2: Types of non-periodic waves.

One of the simplest and most well-known reaction-diffusion equations is

the Fisher equation [9]. It takes the form

$$\frac{\partial u}{\partial t} = D\nabla^2 u + ru^n(u_{\max} - u) \quad (1.2)$$

where D is the diffusion coefficient and r is a constant. It was originally formulated in one-dimension with $n = 1$ to model the propagation of genes, but it also applies to the spread of a population of animals and to autocatalytic reactions of the form



where a and b are the concentrations of A and B , respectively, and k is the rate constant, if the diffusion coefficients of A and B are taken to be the same and the sum of the concentrations of A and B is initially constant in space. Then (1.2) applies with u , r , and u_{\max} replaced by b , k , and $a + b$, respectively. This equation has stable 1-d travelling wave solutions in the form of kinks. In the case of the autocatalytic reaction, the wavefront is the boundary between a region of B and a region of A . Since B consumes A to make more B , the wavefront propagates in the direction of the A region.

The eikonal equation

In two-dimensional systems, the wavefront is a line rather than a point. It can therefore take a variety of shapes. However, there are only three classes of wavefront for which the shape of the wavefront stays the same. These are plane waves, circular waves, and spiral waves [10].

In 2-d reaction-diffusion systems, the local speed of the wavefront approximately obeys the eikonal equation

$$c = c_0 - D\kappa \quad \text{with} \quad |\kappa| = 1/\rho \quad (1.3)$$

where c is the speed of the wavefront at a point, c_0 is the speed of a planar wavefront, and ρ is the radius of curvature of the wavefront at that point. The curvature κ at the point is positive or negative depending on whether the centre of curvature is behind or ahead of the wavefront, respectively (see Fig. 1.3). A plane wavefront has zero curvature (or an infinite radius of curvature) and so

(1.3) reduces to $c = c_0$ in this case, as expected. The direction of the velocity of the wavefront at each point is normal to the tangent plane of the wavefront at that point.

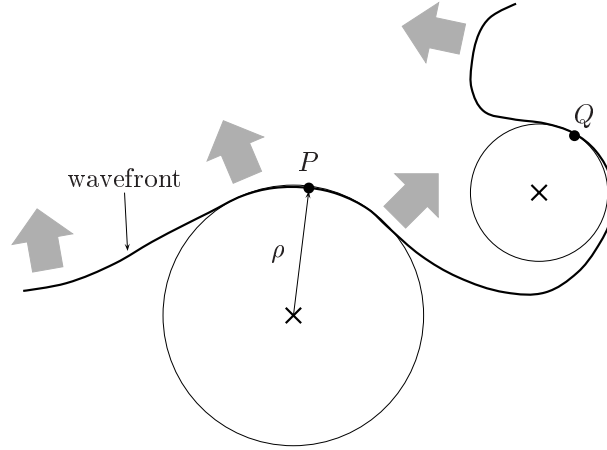


Figure 1.3: Motion of a curved wavefront. Arrows show local direction of motion; crosses are centres of curvature. $\kappa_P > 0$, $\kappa_Q < 0$.

It can be seen that a circular wavefront of radius r travelling outwards will have a speed given by

$$c = c_0 - \frac{D}{r}. \quad (1.4)$$

The speed will be negative if $r < D/c_0$ which means that a circular wave can only propagate if it has a radius larger than

$$r_{\text{crit}} = \frac{D}{c_0}$$

and a circular wavefront can only be formed if the source of the wavefront has a radius larger than r_{crit} .

In three-dimensional systems, wavefronts are surfaces. The obvious 2-d generalizations of wavefronts that maintain their shape are planar, cylindrical, and spherical wavefronts. Generalizations of 2-d spiral waves are known as scroll waves. In general, the local wavefront speed is given by

$$c = c_0 - D(\kappa_1 + \kappa_2) \quad (1.5)$$

where κ_1 and κ_2 are the curvatures at a point on the wavefront measured in

two perpendicular directions. It can be seen that (1.5) reduces to

$$c = c_0 - \frac{2D}{\rho}$$

for a spherical surface of radius ρ (since in that case $\kappa_1 = \kappa_2 = 1/\rho$), and to (1.3) when parallel slices through the wavefront look the same (in which case $\kappa_1 = \kappa$, $\kappa_2 = 0$) e.g. a cylindrical wavefront.

Spiral wave

The simplest type of spiral wave can be described in polar coordinates (r, θ) by

$$\theta = \left\{ \frac{\psi(r) - \omega t + 2\pi n}{m} + \theta_0 \right\} \bmod 2\pi, \quad n = 0, 1, \dots, |m| - 1. \quad (1.6)$$

In the above equation, $2\pi/\omega$ is the period of the pattern, $|m|$ is the number of spiral arms, θ_0 is a phase constant which determines the initial orientation, and ψ is a monotonically increasing function that describes the type of spiral. For example, for an Archimedean spiral,

$$\psi(r) = ar. \quad (1.7)$$

A further requirement for ψ is that $\psi' \rightarrow \text{constant}$ as $r \rightarrow \infty$, which is satisfied by the above example.

The spiral nature of the wavefronts given by (1.6) can be seen by setting $t = 0$. With $|m| = 1$ (which is the most usual case for real systems) θ is single valued ($n = 0$ only) and so there is just one spiral arm. The sign of m determines the direction of the spiral. Positive and negative signs give anticlockwise and clockwise spirals, respectively. With $|m| > 1$, there are $|m|$ symmetrically placed identical spiral arms. Various cases are shown in Fig. 1.4.

As t is increased it can be seen (from both the equation and the figure) that anticlockwise spirals ($m > 0$) will rotate in the clockwise direction, and vice versa. The angular speed of each point on the wavefront will be $\omega/|m|$.

The wavelength λ of a spiral wave is the distance between successive wave-

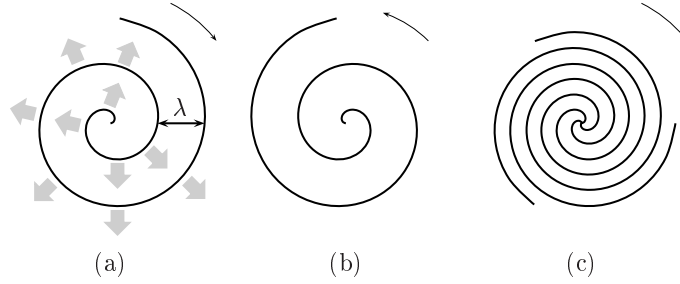


Figure 1.4: Archimedean spiral waves: (a) $m = 1$ (b) $m = -1$ (c) $m = 3$. Filled arrows: local motion of wavefront. Thin arrows: apparent sense of rotation.

fronts in the radial direction. From (1.6), it can be seen that $d\theta = (\psi' dr)/m$ and so

$$m\lambda = \int dr = \int_{\theta_1}^{\theta_1+2\pi} \frac{m d\theta}{\psi'}. \quad (1.8)$$

If $\psi' \rightarrow \psi'_\infty$ as $r \rightarrow \infty$ then for large r this reduces to

$$\lambda_\infty = \frac{2\pi}{\psi'_\infty}. \quad (1.9)$$

For an Archimedean spiral, given by (1.7), $\psi' = \psi'_\infty = a$, and so the wavelength is independent of r for this type of spiral. As r increases, the wavefront becomes less curved and so in the limit of large r , the speed of the wavefront is the plane wave speed $c_0(\lambda_\infty)$ of a periodic wave with wavelength λ_∞ . Since it takes time $T = 2\pi/\omega$ for the wavefront to move one wavelength,

$$c_0(\lambda_\infty) = \frac{\lambda_\infty}{2\pi/\omega} \Rightarrow \omega = c_0(\lambda_\infty)\psi'_\infty. \quad (1.10)$$

There is therefore a relation between the plane wave speed, the type of spiral, and the rate of rotation of the pattern. The type of spiral (i.e. the form of ψ) is determined by substituting (1.6) into the eikonal equation (1.3) with the appropriate boundary conditions. This ends up being a nonlinear eigenvalue problem that must be solved numerically to find ω . The spiral waves from this analysis are found to be approximately Archimedean, in agreement with those seen in nature.

In real systems, the tip of the spiral wave (where the spiral wave starts) is not fixed, but instead (in the simplest cases) moves around a circle known

as the spiral core at the same angular frequency as the rotation of the spiral wave. If this core has radius r_0 , then the $\psi(r)$ given in (1.7) would become $a(r - r_0)$. As will be discussed shortly, for some systems it is also possible for the spiral wave tip to undergo much more complicated motion.

Unlike planar, circular, cylindrical or spherical waves, it is important to note that spiral wave can only exist in systems which have stable pulse-shaped 1-d travelling wave solutions. This is self-evident from the form of these waves. It means that spiral and scroll waves cannot occur in systems such as the simple autocatalytic system described earlier. An important type of reaction-diffusion system where pulse-shaped travelling waves do occur, and hence spiral wave is possible, is the excitable system.

1.2 Excitable systems

Excitable systems are governed by a special class of reaction-diffusion equations. Whether or not a system is excitable depends on the nature of the reaction terms in the equation. We therefore first consider just the state with no spatial variation with the result that the diffusion terms can be ignored.

The simplest type of excitable system can be described by [11]

$$\frac{\partial u}{\partial t} = f(u, v) \quad \frac{\partial v}{\partial t} = \varepsilon g(u, v) \quad (1.11)$$

in which the u -nullcline ($f(u, v) = 0$) has a local maximum and a local minimum, the v -nullcline ($g(u, v) = 0$) intersects $f = 0$ once to give a single stable fixed point (u_*, v_*) , and $\varepsilon \ll 1$. The phase portrait for such a system is shown in Fig. 1.5. A number of properties of the system can be explained by considering the path and speed of trajectories on the phase portrait. First, if a small perturbation is applied (the system is moved away from its steady state by a small amount), the system quickly returns to its steady state. If a large perturbation is applied so that the system is placed on the other side of the threshold, the system will become excited and then slowly return to the steady state. During most of the slow return from the excited state, it is difficult to excite the system again – this is called the refractory phase.

The changes in the v -direction are always slow because of the ε in (1.11).

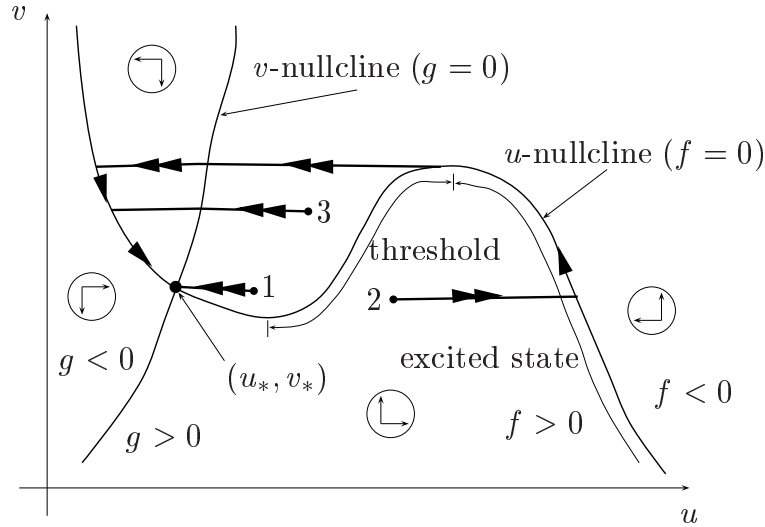


Figure 1.5: Phase portrait for an excitable system with no spatial dependence. Single arrows: slow changes; double arrows: rapid changes; orthogonal arrow pairs in circle: direction of u (right/left) and v (up/down).

The changes in the u -direction are only slow when f is close to zero, which only occurs when the trajectory is close to the u -nullcline.

The quantities u and v are generally known as the activator and inhibitor, respectively. Increasing the amount of activator beyond the threshold will result in the system reaching its excited state. While the system is in the excited state, the activator slowly decreases while the inhibitor slowly increases. When the system leaves the excited state, the activator drops quickly, and then both the activator and inhibitor slowly return to their equilibrium values. The inhibitor is so named because when it is low, the system will quickly become excited, but when the inhibitor level is high, it is more difficult and sometimes impossible for the system to become excited.

Most excitable systems in nature have spatial dependence due to a diffusion term. The simplest are described by reaction-diffusion equations of the form

$$u_t = D_u \nabla^2 u + f(u, v) \quad v_t = D_v \nabla^2 v + \varepsilon g(u, v) \quad (1.12)$$

where D_u and D_v are the diffusion coefficients of the activator and inhibitor, respectively. In many systems, $D_v \simeq 0$.

To investigate the form of the travelling wave solutions in one dimension it is most convenient to transform to a frame moving at the same speed as a

wave moving to the left. If the wave is travelling at speed c this means writing $z = x + ct$. This gives, after rearranging,

$$u_z = \frac{1}{c} \left(f(u, v) + D_u \frac{\partial^2 u}{\partial z^2} \right), \quad v_z = \frac{1}{c} \left(\varepsilon g(u, v) + D_v \frac{\partial^2 v}{\partial z^2} \right). \quad (1.13)$$

It is not possible to do proper phase plane analysis on this system as it is four-dimensional. However, apart from the diffusion terms, these equations have the same form as (1.11) with the t replaced by z/c . This means that the shape of the travelling wave will be similar to the time dependence of the spatially independent system if the diffusion terms are small compared with f and g for most of the time. The form of the travelling wave is shown in Fig. 1.6.

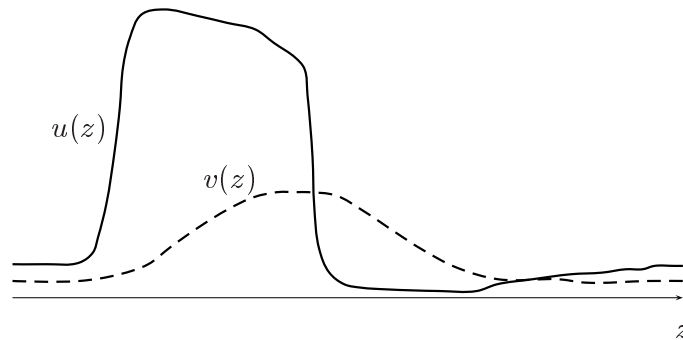


Figure 1.6: Travelling wave in an excitable system. The wave is moving to the left.

Behind and ahead of the travelling wave u and v are at their equilibrium values. The activator concentration starts increasing at the start of the wave due to a large positive $\partial^2 u / \partial z^2$ which is enough to make $u_z > 0$ in spite of the fact that $f < 0$. Once past the threshold, u rapidly rises until it reaches the excited state after which it drops slowly while v increases. As with the spatially independent case, it will leave the excited state, with u dropping very quickly. However, when this happens $\partial^2 u / \partial z^2$ will be large and negative which means that it will leave the excited state at a lower value of v than illustrated in Fig. 1.5, and consequently ‘cut across’ the $f > 0$ region. Finally, at the tail of the wave, u and v slowly return to their equilibrium values. A similar analysis starting with $z = x - ct$ will show that a mirror image of this wave travelling to the right is also possible.

To start a travelling wave of this type, an excess of activator must be supplied to a localized region. If the excess is too small, the excited state will not be reached and the excess will quickly decrease as a result of both the reaction and diffusion terms. Travelling waves will only be generated if the excess is large enough so that the excitable state is reached, and in higher-dimensional cases, the size of the region must also exceed a certain critical radius as was discussed earlier. In one dimension, two travelling waves moving apart in opposite directions will form. In two or three dimensions, a symmetrical initial region of excess activator will generate a circular or spherical wave, respectively. Spiral waves are generated by removing part of a wavefront – the two ‘free ends’ so created will form the tips of a pair of spiral waves rotating in opposite directions.

The refractory phase of excitable systems means that excitable waves have what is known as a refractory tail. In this region it is impossible to have another excitable wave. This has two important consequences. First, there is a minimum wavelength for a periodic train of excitable waves – the trailing wavefront can only follow the leading wavefront at a distance larger than the length of the refractory tail. Second, wavefronts are annihilated when they collide or hit a boundary. There is no possibility of reflection or the waves passing through one another due to the refractory tails.

It should be noted that these waves are of permanent form – their amplitude or functional form does not change with time. This is also true of the higher-dimensional generalizations of these waves. Also, the periodic trains of waves mentioned above have a similar form to the single waves. In this case, the speed of propagation depends on the wave period. The speed decreases slightly with decreasing wavelength until there is a sudden cut-off at the critical wavelength below which periodic wavetrains cannot exist.

Excitable systems in nature in which spiral waves have been observed include the Belousov-Zhabotinsky (BZ) reaction [12], catalytic oxidation on surfaces [13], slime mold [6], heart muscle [5] and mammalian neocortex [14].

1.3 Motion of the spiral tip

The motion of spiral wave tip can be classified as being either simple rotation or compound rotation. In simple rotation, also known as rigid rotation, the tip rotates around a fixed circular core and the angular velocity is constant [15]. This type of motion is therefore strictly periodic. In compound rotation, also known as meandering, the spiral tip rotates with two frequencies [16]. If the two frequencies are incommensurate, the path of the tip will never repeat itself and the motion is quasiperiodic. There are two types of meandering. In one type, the spiral tip moves in epicycloidal trajectory (inward petals) and in the other it has hypocycloidal motion (outward petals), as shown in Fig. 1.7. In general, meandering spirals are more often observed than rigid rotating spirals [17, 18]. The variety of possible types of motion as a function of the system parameters for a generic excitable system is shown in Fig 1.8.

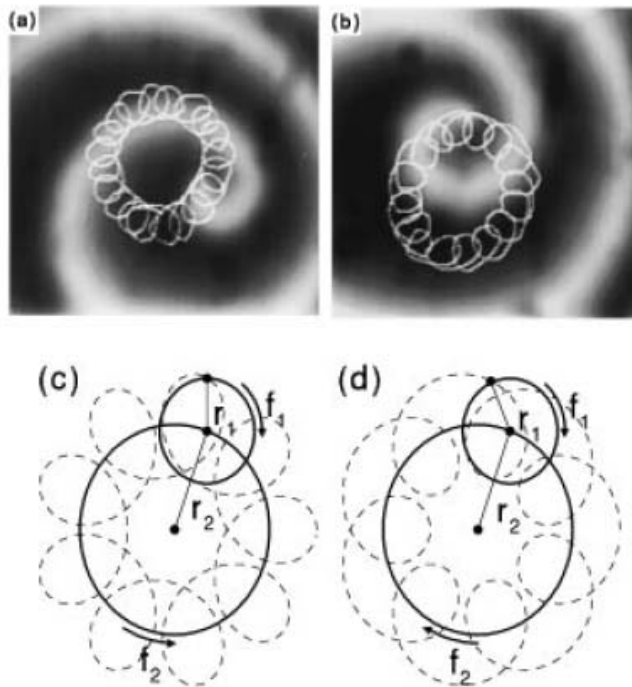


Figure 1.7: Meandering spiral with (a) outward and (b) inward petals. The white lines in the images show the trajectories of spiral tip. (c) and (d) illustrate, respectively, a hypocycloidal and epicycloid, analogous to the motion in (a) and (b). (From [19]).

Experiments [22, 23] and theoretical analysis [24] have shown that whether

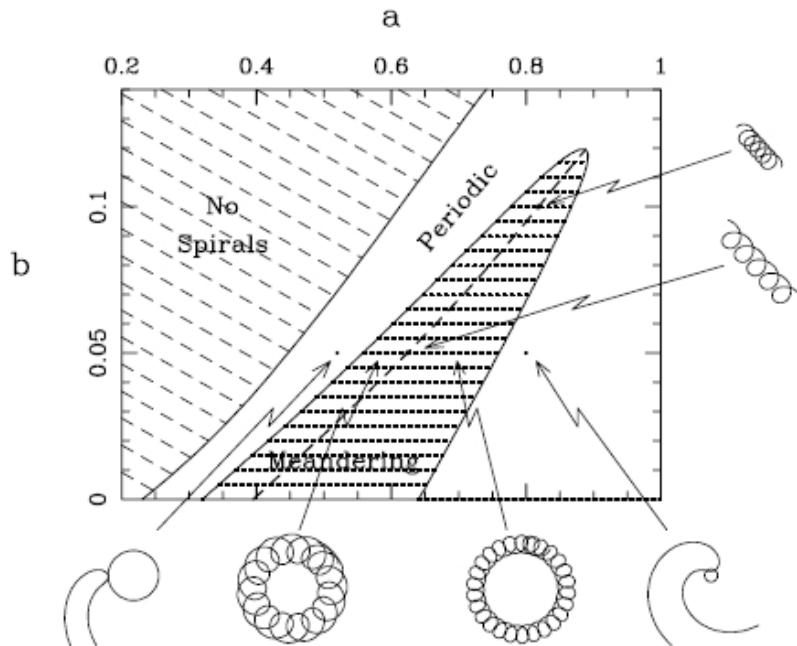


Figure 1.8: Phase diagram or flower garden of spiral dynamics and a function of two control parameters (a and b) in a reaction-diffusion model of Fitzhugh-Nagumo type [20]. There are three main parameter regions containing: no spiral waves, periodically rotating spirals, and meandering spiral waves. The meander region is itself separated into regions whose flowers have inward petals and outward petals by the dashed curve (from [21]).

rigid rotation or meandering occurs depends on the excitability of the system [25, 17]. Rigidly rotating spirals tend to be observed when the system has either a very high or very low excitability. Excitability is a measure of how close the threshold is to the stable steady state. If a system parameter controlling the excitability is varied periodically in time, in addition to cycloids, tip trajectories in the form of ‘wavy cycloids’ and Lissajous figures are obtained [26, 27, 28]. If the period of the variation in excitability is exactly the same as the period of the spiral wave rotation, then the spiral core will move in a straight line. This is known as resonant drift [29]. The direction of the drift depends on the relative phase of the spiral wave and the excitability variation. This would appear to be a straightforward method to control the spiral wave. As spiral waves occur in a malfunctioning heart [30], a strategy for removing the wave might be to somehow apply a modulation of the excitability with the same period as the spiral wave so that the wave is moved to a boundary and

disappears. However, it has been shown that such resonantly drifting spiral waves are repelled by boundaries [31]. This difficulty could be overcome by applying the variation of the excitability in response to the measured value of the state of the system at a point or over a region of the excitable medium. This is known as feedback control.

1.4 Spiral wave dynamics under feedback control

The motion of the spiral core has been studied under a number of different types of feedback regimes. These can be divided into two classes – local feedback and non-local feedback. Local feedback is where the excitability of the system is modulated according to the state of the system at a single point. In non-local feedback, the system excitability is modulated in response to the state of the system at more than one point – normally the average value over a region.

The effect of feedback has been investigated experimentally [32, 33, 34, 35], numerically [26, 36, 37], and theoretically [38, 39, 40]. In the experimental studies and some of the numerical simulations, the excitable system used was the BZ reaction with a light-sensitive catalyst. For this system, the excitability is a function of the applied light intensity. This light is applied homogeneously over the whole system. In the remainder of the numerical studies, an idealized excitable system model was used [37]. Further details will be given in later sections.

Local feedback

In local feedback (also known as one-channel feedback), an arbitrary point in the medium is selected and the excitability of the system is then modulated according to the state of the system at that measuring point. It is found that the trajectory of the spiral core centre is attracted to a series of circular limit cycles centred on the measuring point [26]. If the measuring point is selected such that it is near to the spiral tip before feedback is applied, the spiral tip will end up on the innermost limit cycle. Otherwise, it will end up on a limit

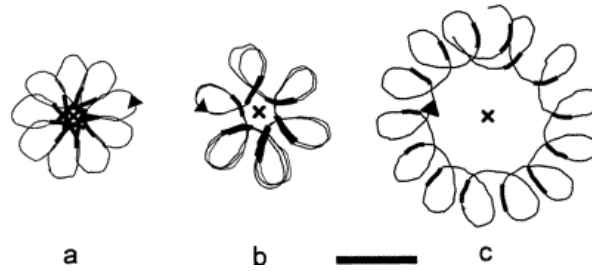


Figure 1.9: Experimentally determined entrainment attractors for various time delays, τ : (a) $\tau = 0$ s (b) $\tau = 3$ s (c) $\tau = 5$ s. Thick segments of the trajectories are when the increased light intensity was applied. Scale bar: 0.5 mm. (From Ref. [27])

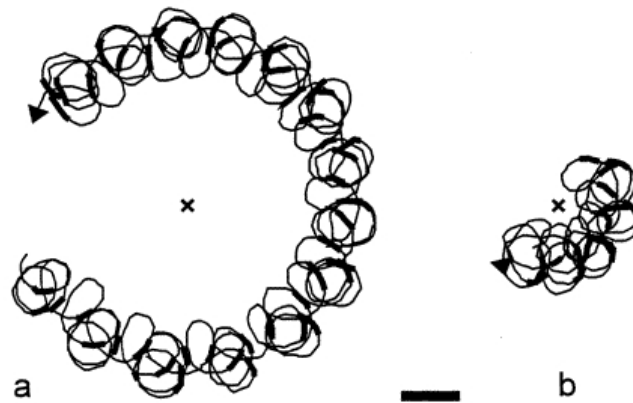


Figure 1.10: Experimentally determined resonance attractors for various time delays, τ : (a) $\tau = 7$ s (b) $\tau = 25$ s. Scale bar: 0.5 mm. (From Ref. [27])

cycle further away. If the motion on the innermost limit cycle is epicycloidal then this limit cycle is referred to as the entrainment attractor while the limit cycles further from the measuring point are known as resonance attractors [41]. If the spiral is meandering before feedback is applied, the innermost limit cycle will be an entrainment attractor and is illustrated in Fig. 1.9. On a resonance attractor, the meandering spiral core has a four loop drift along the circular limit cycle as shown in Fig. 1.10.

The feedback can be applied with a time delay, τ . As can be seen in Figs. 1.9 and 1.10, the value of τ affects the radius of the attractor. The influence of one-channel feedback on a rigidly rotating spiral has also been studied experimentally [42]. The effect of time delay on the size of resonance attractor is shown in Fig 1.11. It shows the drift of the spiral wave core along a

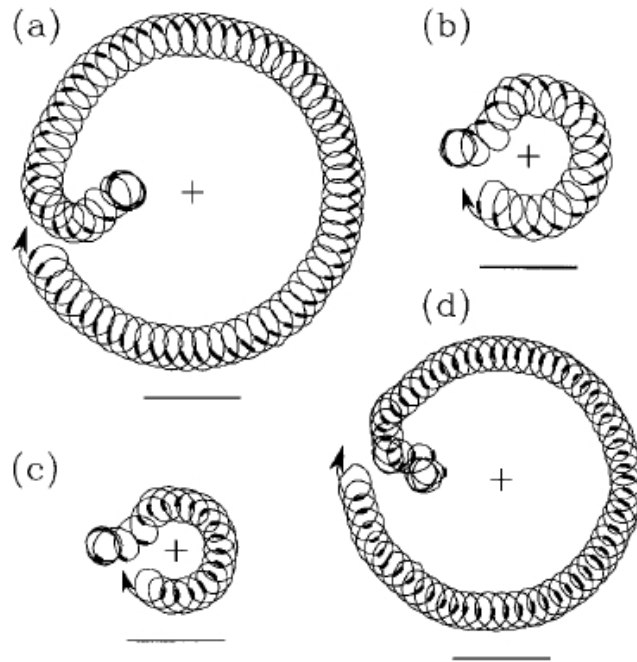


Figure 1.11: Trajectories of the spiral wave tip (thin solid line) observed for different time delays τ and feedback light-pulse amplitudes A : (a) $\tau = 5$ s, $A = 0.08$ mW/cm², (b) $\tau = 30$ s, $A = 0.08$ mW/cm², (c) $\tau = 5$ s, $A = -0.08$ mW/cm², (d) $\tau = 35$ s, $A = -0.08$ mW/cm². Scale bar: 1 mm. (From Ref. [42])

stable circular orbits centred at the measuring point. The theory of resonance attractors given in Ref. [43] is in good agreement with these results.

Finally, if there is a sufficient time delay between the measuring point state and the modulation of the excitability, the limit cycles become unstable in favour of attractors of a more complicated nature [35].

Non-local feedback

The most obvious generalization of one-channel feedback is to instead monitor the state of the system at two points and add the signals from both to determine the strength of the feedback signal. It has been shown that this two-channel feedback destroys the regular dynamics seen in one-channel feedback if the measuring points are sufficiently far apart. Several complex regimes are found on varying the distance between the two measuring points [44]. Of particular interest is the appearance of lines along which the spiral wave core

does not drift at all [45]. These are illustrated in the spiral core drift velocity plot shown in Fig. 1.12.

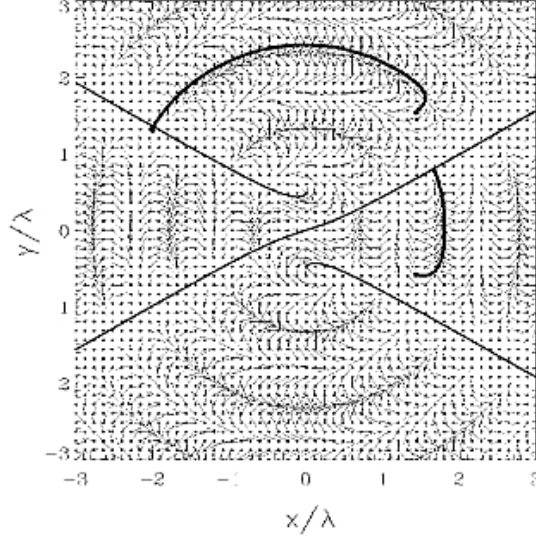


Figure 1.12: Spiral core drift velocity fields for two-channel feedback when the distance between the measuring points is equal to wavelength of the spiral wave. Thick solid lines: trajectories of the spiral core. Thin solid lines: locus of points where the drift velocity is zero. (From Ref. [45])

In the other types of non-local feedback studied so far, the excitability is modulated according to the expression

$$I(t) = I_0 + k_{fb}\{B(t - \tau) - B_0\}, \quad (1.14)$$

where I_0 and the feedback gain k_{fb} are constants and

$$B(t) = \frac{1}{S} \int_D g(x, y, t) dx dy \quad (1.15)$$

where S is the area of the sensory domain D over which the integration of the state variable g is performed. B_0 is the average value of $B(t)$ over one revolution of a spiral wave located at the centre of the domain. In the experiments involving the photosensitive BZ reaction, $I(t)$ is proportional to the applied light intensity and I_0 is then the background light intensity when no feedback is applied [46, 47].

It has been found in various studies that when the domain size is sig-

nificantly smaller than the wavelength, λ , of the spiral wave, the spiral core trajectories are similar to those for local feedback. However, for larger domains, the nature of the attractors depends very much on the size and shape of the domain [39, 48]. The change in behaviour occurring as a function of domain size has been examined for circular [47] and square [39, 49] domains.

The simplest type of behaviour is seen with circular domains. This is to be expected since the system has full rotational symmetry about the centre of the domain in this case. Both experimental and numerical results show that the final trajectory of spiral wave core is in circular path around the circular domain. Some experimental results for this are shown in Fig. 1.13. In fact for any size of domain, the core trajectory will finally tend to either a stable fixed point at the centre of the domain or a circular limit cycle concentric with the domain.

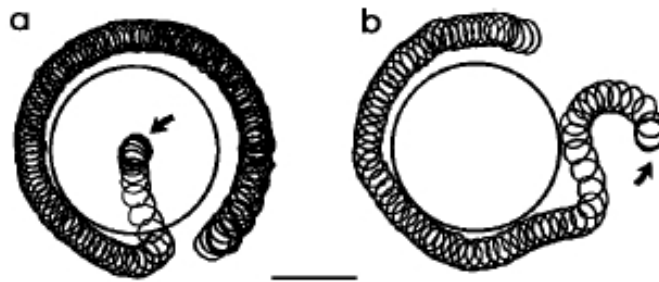


Figure 1.13: Trajectories of the spiral wave tip under positive feedback with time delay $\tau = 0$ observed for different initial locations of the spiral wave core (arrows): (a) at the centre and (b) outside of integration area. Scale bar: 1 mm. (From Ref [50])

The behaviour for other domain geometries with less symmetry is more complex. For example, for an elliptical domain as shown in Fig. 1.14, the resonance attractor can be destroyed due to a saddle-node bifurcation induced by a variation of the domain eccentricity [36].

For a square domain of size λ , the core drifts in an approximately square path around the domain as can be seen in Fig. 1.15. As the size of the square domain is increased, the number of fixed points in the drift velocity field increases [49, 36]. These fixed points are found to lie on a fairly regular lattice inside the domain.

A wide variety of other domain geometries have been looked at, but not

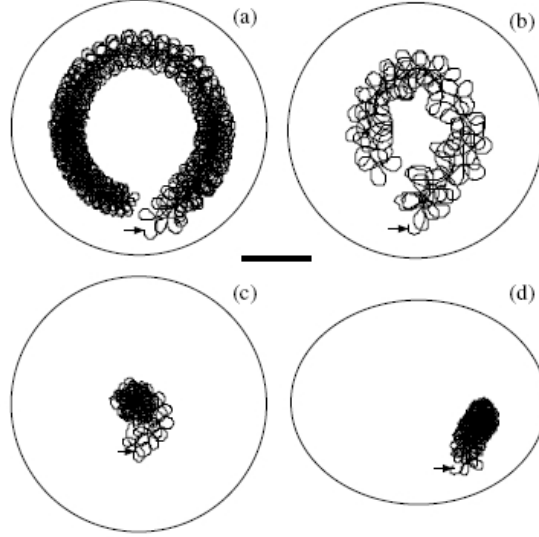


Figure 1.14: Resonant drift of a spiral wave induced by a global feedback with $k_{fb} = -1.5$, $B_0 = 25$, and $I_0 = 70$. (a)-(c) Circular domain of radius $R = \lambda$; (d) elliptical domain with large axis $a = 2\lambda = 4$ mm and small axis $b = a/1.25$. In (a) and (d), the time delay is $\tau = 0$, in (b) $\tau/T_\infty = 0.5$. Initial spiral tip locations are marked by arrows. Scale bar: 1 mm. (From [36])

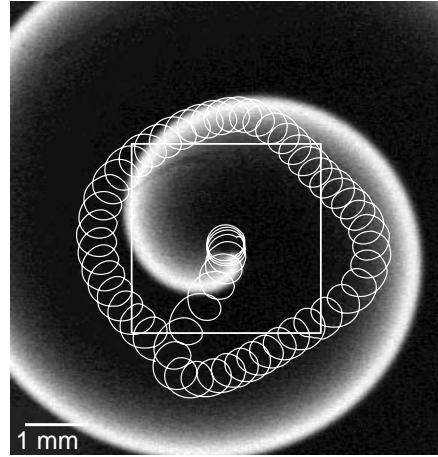


Figure 1.15: Trajectory of spiral wave in square path around the centre of square domain. Domain size: 1λ

in so much detail [48]. Some of the numerically obtained trajectories are illustrated in Fig. 1.16. It is to be noted that in some cases the trajectory has the same shape as the domain when the domain has a specific size (square domain: 1λ , triangular domain: 1.4λ).

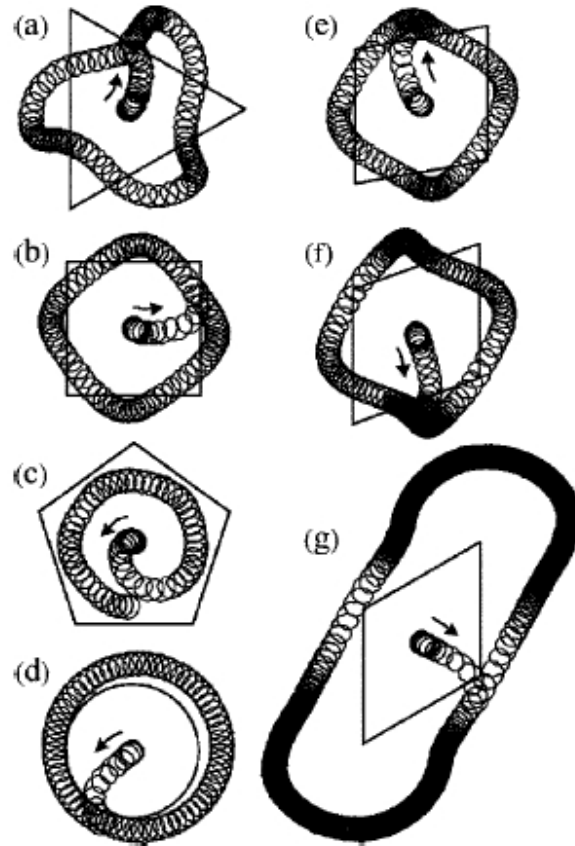


Figure 1.16: Trajectories of the spiral wave tip with different shape of sensory domain (a) Triangle side length 1.5λ , (b) square side length 1.0λ , (c) pentagon side length 1.0λ (d) circle, diameter 1.0λ (e-g) rhombus side length 1.0λ acute angle: 80° , 70° and 60° respectively (from [48]).

1.5 The light-sensitive Belousov-Zhabotinsky reaction

The excitable system that we will use to study the effect of feedback on spiral wave core trajectories is the light-sensitive Belousov-Zhabotinsky (BZ) reaction. The reaction involves the oxidation of malonic acid by bromate producing carbon dioxide in a medium of sulphuric acid [51]. Depending on the concentrations involved, the reaction can be made to show relaxation oscillations or behave as an excitable system. The changes can be observed through the colour of the solution. The colour (and the light-sensitivity) depends on the type of catalyst used.

The BZ reaction is rather complicated. To understand the most important steps, we review the simplified mechanism given by Field, Körös and Noyes (FKN) [52]. This FKN mechanism can be described as three processes as shown in Table 1.1.

Process A
(R1) $\text{Br}^- + \text{HOBr} + \text{H}^+ \rightarrow \text{Br}_2 + \text{H}_2\text{O}$
(R2) $\text{HBrO}_2 + \text{Br}^- + \text{H}^+ \rightarrow 2\text{HOBr}$
(R3) $\text{BrO}_3^- + \text{Br}^- + 2\text{H}^+ \rightarrow \text{HBrO}_2 + \text{HOBr}$
Process B
(R4) $2\text{HBrO}_2 \rightarrow \text{BrO}_3^-$
(R5) $\text{BrO}_3^- + \text{HBrO}_2 + \text{H}^+ \rightarrow 2\text{BrO}_2 + \text{H}_2\text{O}$
(R6) $\text{BrO}_2 + \text{Cat}_{\text{red}} + \text{H}^+ \rightarrow \text{HBrO}_2 + \text{Cat}_{\text{ox}}$
Process C
(C1) $\text{CH}_2(\text{COOH})_2 \rightleftharpoons (\text{HO})_2\text{C} = \text{CHCOOH}$
(C2) $(\text{HO})_2\text{C} = \text{CHCOOH} + \text{Br}_2$ $\rightarrow \text{BrCH}(\text{COOH})_2 + \text{H}^+ + \text{Br}^-$
(C3) $2\text{Cat}_{\text{ox}} + \text{CH}_2(\text{COOH})_2 + \text{BrCH}(\text{COOH})_2$ $\rightarrow f\text{Br}^- + \text{other products}$

Table 1.1: Abbreviated FKN mechanism governing the BZ reaction.

In process A, the reduction of bromate to bromine via the reducing agent bromide occurs. In this step, bromomalonic acid is also produced. Then the concentration of bromide eventually falls below some critical level. When it reaches the critical value, process B starts to become more important. The hypobromous acid (HBrO_2) begins to compete with the bromide to reduce the bromate. This increases with an accelerating rate and the oxidized form of the catalyst is produced. This results in a sudden colour change for a suitably chosen catalyst (and indicator). In process C, the catalyst formed from Processes A and B reverts to its reduced form and Br^- is produced.

The HBrO_2 is the autocatalytic species in the reaction. Without another process occurring to remove this species, the autocatalyst would form a kink type wave (Fig. 1.2(b)). It turns out that process B is inhibited when the amount of bromide is high. Thus bromide acts as the inhibitor for the autocatalyst.

A light-sensitive ruthenium tris-bipyridyl complex $\text{Ru}(\text{bpy})_3^{2+}$ is used as a catalyst for the excitable system in order to control or study the behaviour

of the system by using intensity of light [53]. Illumination at around 452 nm produces an excited state of the ruthenium catalyst. Light decreases the velocity and even inhibits wave propagation completely [54]. The inhibitory effect of light on the ruthenium-catalyzed BZ reaction is associated with additional bromide production in accordance with the photochemical properties of the ruthenium complex [55].

1.6 Outline

The spiral waves are an interesting pattern in excitable media. They have been observed in biological, chemical and physical systems. In the case of biological systems such as the aggregation of slime mold *Dictyostelium discoideum* cells and heart muscle, the spiral waves occur when the cells are in trouble and about to die. For instance, spirals in cardiac muscle are believed to play a vital role in life-threatening situations such as tachycardia and fibrillation. Spiral waves also appear in aggregating slime mold cells when the cells are starving and going to die. It is therefore of interest to seek some effective methods for spiral wave control.

To study the behaviour of spiral wave and try to control them, the light-sensitive Belousov-Zhabotinsky (BZ) reaction is a very powerful tool to observe the spiral wave in the laboratory. The control of spiral waves in light-sensitive BZ reaction can take the form of periodic forcing, one-channel feedback and non-local feedback which induces the spiral wave move on a linear path, entrainment or resonance attractor. For non-local feedback, feedback using the signal integrated over circular and square domains has been observed. Stable nodes, unstable nodes and limit cycles are found inside the domain. It would appear that other types of geometry domain could give rise to additional interesting phenomena. The objective of this work is to study the influence of non-local feedback via an triangular domain on the dynamics of spiral waves. In this thesis we present both experimentally and numerically derived results for the case of feedback control of rigidly rotating spiral waves using domains in the shape of equilateral and isosceles triangles. The fact that in this case each vertex is opposite a side turns out to be crucial. It results in significant differences in the shape of the limit cycles and a more complicated sequence of

bifurcations as compared with those obtained with a square domain. We also develop a simplified model, which we refer to as the plane wave approximation. We use this to account for the locations of regions outside the domain where the core has an exceptionally large or small speed. We call these regions express and stagnation zones, respectively.

The remainder of this thesis is organized as follows. In Chapter 2 details are given of how the BZ reaction we use is prepared. The experimental setup used to illuminate the reactants, gather data and apply feedback is explained, along with some details of the controlling program. Chapter 3 contains a description of the equations we use for the computational analysis of an excitable system under feedback. It also deals with the numerical method for solving the equations, and obtaining the drift velocity vector field plots. Finally, we give a new way of presenting the vector field data, the divergence plot, which greatly eases their interpretation. In Chapter 4 the plane wave approximation is formulated. The experimental and computational results for feedback via equilateral and isosceles triangular domains are given in Chapter 5. The plane wave approximation is used to account for the behaviour seen far from the domain. In the final chapter, the key results of this are summarized and their application and possibilities for further work are considered.

Chapter 2

Experimental Part

In this chapter we describe the experimental setup, preparation of chemicals and observation techniques. The experimental observations were carried out in using a photosensitive Belousov-Zhabotinsky (BZ) reaction. The reaction is observed in a gel in a Petri dish. The recipe of the BZ reaction, the concentration of the catalyst and the thickness of the gel layer were chosen in such a way that it is possible to generate a rigidly rotating spiral wave. The illumination of the system and image analysis were computer controlled.

2.1 Preparation of chemicals

Commercially available analytical grade reagents (malonic acid, sulphuric acid, sodium bromide and sodium bromate) were used for the preparation of the BZ stock solutions. The light-sensitive catalyst, $\text{Ru}(\text{bpy})_3^{2+}$ at a concentration of 4.2 mM was immobilised in a 0.33 ± 0.02 mm silica gel layer at the base of a 7 cm diameter Petri dish. All the solutions were prepared using distilled, deionized water.

Preparation of $\text{Ru}(\text{bpy})_3\text{SO}_4$

$\text{Ru}(\text{bpy})_3\text{SO}_4$ is not available for purchase so it is prepared by precipitation from tris (2,2'-bipyridine) ruthenium (II) chloride [$\text{Ru}(\text{C}_{10}\text{H}_8\text{N}_2)_3\text{Cl}_2 \cdot 6\text{H}_2\text{O}$] in sulphuric acid. Initially, 2.5 g of $\text{Ru}(\text{bpy})_3\text{Cl}_2$ are dissolved in 40 ml of water and then made up to 100 ml with 5 M sulphuric acid. $\text{Ru}(\text{bpy})_3\text{SO}_4$ is formed

as a reddish crystals. After 3 hours the crystals are filtered out and then dried at 50°C for two days. Note that the filter paper must be discarded before putting the sediment into the oven otherwise the sediment will get burned by the burning filter paper. The Ru(bpy)₃SO₄ obtained was dissolved in 100 ml of 0.025 M sulphuric acid. The precise concentration of Ru(bpy)₃SO₄ in this solution was measured spectrophotometrically [55]. In order to avoid inaccuracies in calculating the concentration, the absorption value must be under 1.0 unit. The solution is therefore diluted 500 times by adding 0.01 ml of Ru(bpy)₃SO₄ to 4.99 ml of 0.025 M sulphuric acid. Then an aliquot of the resulting solution is transferred into a cuvette with a light pathway of 1 cm. The 0.025 M sulphuric acid is used as a blank solution. The absorption of the spectrum at 460 nm is measured. The concentration c of Ru(bpy)₃SO₄ is calculated from

$$c = \frac{A}{2\epsilon d}$$

where A is the absorption value, d is the width of the cuvette, ϵ is the extinction coefficient of the complex at the specific wavelength. The width of the cuvette used was 1.0 cm, and for ruthenium II at 460 nm, $\epsilon = 13.4 \times 10^3 \text{ M}^{-1}\text{cm}^{-1}$ [56].

Preparation of the Ru(bpy)₃²⁺ catalyst silica gel

The stock solutions of waterglass (sodium silicate) were prepared by dissolving the appropriate amount of sodium trisilicate (Na₂Si₃O₇, Fluka: Na₂O 18%, SiO₂ 60%) in distilled water [57]. We used 13% waterglass which was prepared by adding 15 g of sodium trisilicate to 100 ml of distilled water. To dissolve the mixture, it was kept hot while stirring intensively until the solution was transparent. After cooling down to room temperature, the solutions was filtered and the amount of water lost due to evaporation was re-added.

In order to fix the concentration of the ruthenium catalyst in the gel at 4.2 mM, the relative volumes of Ru(bpy)₃SO₄ solution and waterglass must be adjusted. The silica gel is obtained by preparing 1 ml of the mixture of 5 M sulphuric acid, distilled water and Ru(bpy)₃SO₄. As the volume of Ru(bpy)₃SO₄ is fixed, the amount of sulphuric acid and water must be adjusted. How fast the solution becomes a gelatinous mass depends on the amount of sulphuric acid (the larger the amount, the faster the gelation). If gelation is too fast

or too slow, the volume of sulphuric acid has to be decreased or increased, respectively, and the volume of water also has to be changed correspondingly. The mixture of sulphuric acid, water and $\text{Ru}(\text{bpy})_3\text{SO}_4$ was then slowly added to 2 ml of the 13% waterglass solution while stirring. Then 2 ml of the mixture is poured into a Petri dish to gelate. Since the homogeneity of the gel layer is important, the Petri dish is placed on a horizontal glass plate. It was ensured that the plate was horizontal by using a spirit level. The thickness of the gels was measured using a micrometer and found to be 0.33 ± 0.02 mm.

During gelation the pH of the gels increased. For neutralisation it is necessary to cover the gel first with 6 ml of 0.1 M sulphuric acid for about 30 minutes and then several times with a large amount of distilled water. The ready-to-use gels were kept under distilled water. A typical example of the recipe for preparing the silica gel in this study is as follows:

0.20 ml	H_2O
0.70 ml	0.018 M $\text{Ru}(\text{bpy})_3\text{SO}_4$
0.10 ml	5 M H_2SO_4

Preparation of the BZ reaction

The stock solutions used for making the BZ reaction are listed in Table 2.1.

reagent	company	quantity
1 M NaBrO_3	Riedel-de Haen, 99.5%	15.089 g NaBrO_3 in 100 ml H_2O
4 M MA^1	Merck, 99%	41.624 g MA in 100 ml H_2O
5 M H_2SO_4	Riedel-de Haen	standard solution
1 M NaBr	Riedel-de Haen, 99.5%	10.289 g NaBr in 100 ml H_2O

Table 2.1: The stock solutions used to prepare the BZ reaction.

The investigation of wave propagation needs a few hours but the lifetime of a rigidly rotating spiral wave in a closed system is short. To maximize the lifetime, a reservoir layer of BZ solution is placed above the $\text{Ru}(\text{bpy})_3^{2+}$ catalyst silica gel. The excitable system is prepared from two different BZ solutions that we refer to as BZ1 and BZ2 [58]. The concentrations of the reagents in

¹Malonic acid

BZ2 are half of those in BZ1. Solution BZ2 is put onto the gel a few minutes after BZ1 in order to enlarge the reservoir of the reaction. The quantities and reagents used in the preparation of the two solutions are given in Table 2.2.

reagent	quantity (ml) BZ 1	quantity (ml) BZ 2
NaBrO ₃	0.90	1.80
MA	0.21	0.42
H ₂ O	0.55	6.10
H ₂ SO ₄	0.39	0.78
NaBr	0.45	0.90

Table 2.2: Quantities and reagents used to prepare the two BZ solutions.

The BZ solutions are prepared by first adding the malonic acid to the sodium bromate followed by the water and sulphuric acid. Addition of the sodium bromide to this must be done under a fume hood, as some bromine gas is evolved which is toxic. After the sodium bromide is added, the solution which is originally colourless turns yellow because in an acidic environment bromate is oxidised by bromide to form yellowish bromine. The bromination of the malonic acid results from the presence of bromine. After around 5 minutes the solution becomes colourless again.

To start the reaction, 2 ml of the BZ1 solution is put on top of the gel in which the catalyst is immobilized. The solution is left for a few minutes to allow the concentrations of the reagents in gel and solution to attain homogeneity through diffusion. Since the volume of BZ1 solution added is the same volume as the volume of the gel, the overall concentration of the BZ solution will be half that of BZ1. It will therefore be the same as the concentration of the BZ2 solution. The reservoir of BZ solution above the gel is then enlarged by adding 8 ml of the BZ2 solution onto the gel. After equilibrium is established the calculated concentrations of the reactants are given in Table 2.3.

2.2 Generation of a single spiral wave

To create a single spiral wave in the Petri dish, the BZ solution is first poured on the gel at the boundary of the Petri dish. The inhomogeneities at the edge of the dish act as source of a semi-circular oxidation wave (Fig. 2.1a). This

reagent	concentration (M)
NaBrO ₃	0.20
MA	0.17
H ₂ SO ₄	0.39
NaBr	0.09

Table 2.3: The concentrations of the BZ reactants

wave moves slowly to the centre of the dish. A spiral wave is generated by removing half of the semi-circular wavefront when it has reached the centre of the dish (Fig. 2.1c). This is done by using a cold light source which provides a 4 mm diameter circular spot of high illumination intensity which completely suppresses the wave activity. Half of the wave is deleted by moving the light spot along the wavefront from the centre to the boundary. The remaining open end evolves into a single rotating spiral wave near the centre of the dish (Fig. 2.1d). In order to obtain an anticlockwise spiral wave, the right-hand side of the wavefront is removed as viewed from behind the wavefront as illustrated in Figure 2.1.

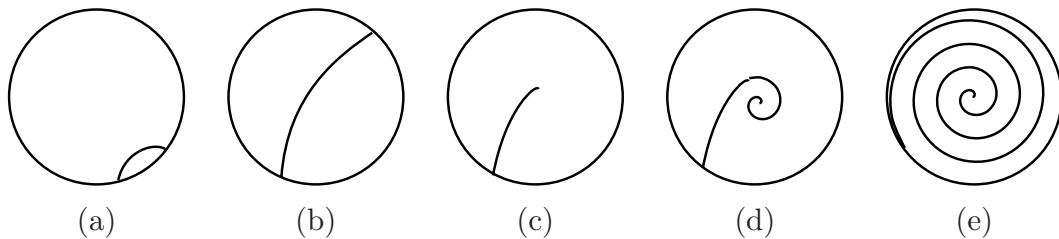


Figure 2.1: Creation of an anticlockwise spiral: (a) A semi-circular wave is created at boundary of the Petri dish (b) wave moves to the centre of the Petri dish (c) half of wavefront is deleted (d) the open end starts to form a spiral wave (e) the complete anticlockwise spiral wave

The spiral wave is allowed to fully form before feedback is applied. An unperturbed spiral wave prepared in this way has an initial wavelength of 2.1 to 3.0 mm and a period of 52 to 60 s. The spiral wavelength was monitored continually. In some cases the wavelength was found to increase with time. When nonlocal feedback is being applied, an increase in the wavelength is equivalent to a decrease in the size of the domain. As this effect was not desired, the recorded tip trajectory from time at which the wavelength started to increase significantly had to be discarded.

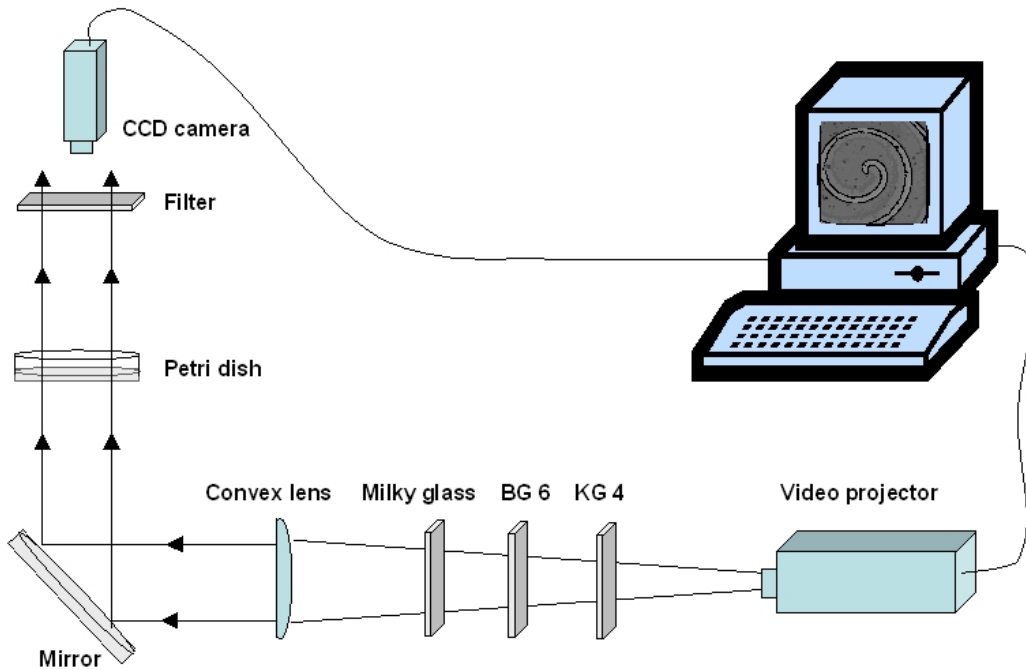


Figure 2.2: The experimental setup

2.3 Experimental setup

The experimental setup is shown in Figure 2.2. The central $3\text{ cm}\times 3\text{ cm}$ region of the Petri dish is monitored using a Hamamatsu H 3077 CCD camera connected to a computer. The waves appear blue on an orange background. To facilitate the image processing, the contrast between wavefront and background is enhanced by placing a $490\pm 13\text{ nm}$ filter in front of the camera. The Petri dish is illuminated from below by a Panasonic PT-L555E video projector whose light intensity is controlled by a computer. To illuminate the Petri dish, the light from the video projector is reflected up to the Petri dish by a mirror. The KG4 filter removes infra-red radiation to minimize the heating of the solution from the light beam. The BG6 filter passes wavelengths of $310\pm 530\text{ nm}$ as the Ru catalyst is most sensitive to this range [53]. The milky glass and convex lens (focal length 22 cm) ensure that the beam is homogeneous and collimated, respectively. The Petri dish can be adjusted in the vertical and horizontal directions by a micro-manipulator.

The CCD camera output is connected to a frame grabber card (Data Translation DT3155) in the computer. The frame grabber digitizes the analogue

signal from the camera. The frame grabber data is read by a program which controls the light output from the video projector. An image in the form of a homogeneous grey region is sent to the video projector. The light intensity at the Petri dish as a function of the grey level was measured using a Tektronix J 1812 photometer. The results are shown in Fig 2.3. Grey levels of 0 and 255 correspond to black and white, respectively. The light intensities used lie in the linear response region of the video projector between 0.7 to 1.7 W/m². In this region, corresponding to grey levels between 100 to 170, a change of grey level of 1 unit, corresponds to a change in intensity of 20 mW/m².

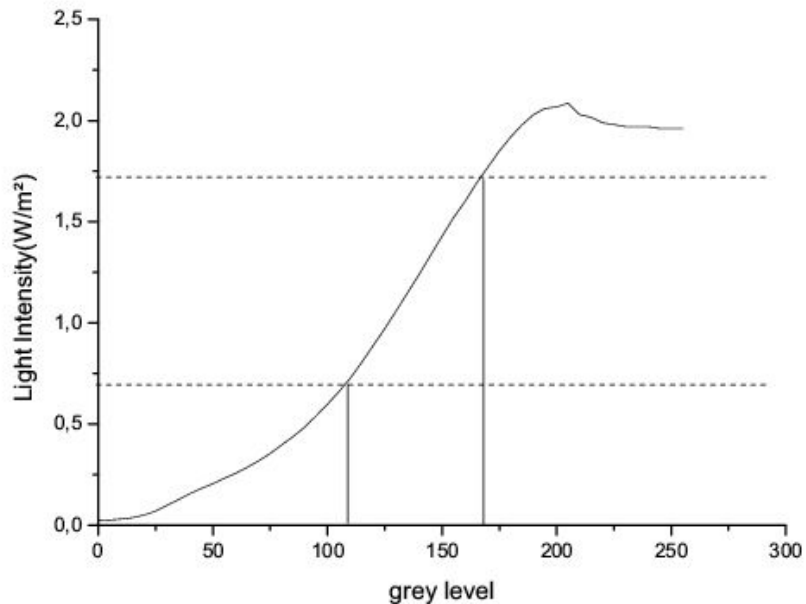


Figure 2.3: Light intensity at Petri dish versus grey level sent to the projector

2.4 Controlling program

To apply feedback, a controlling program takes the digitized image from the frame grabber card and computes the desired intensity level, $I(t)$, according to

$$I(t) = I_0 + k_{fb}(B(t) - B_0), \quad B(t) = \frac{1}{S} \int_D g(x, y, t) dx dy \quad (2.1)$$

where k_{fb} is the feedback gain, S is the area of the sensory domain D over which the integration of the image brightness g is performed, and B_0 is the

average value of $B(t)$ over one revolution of a spiral wave located at the centre of the domain. The program also controls the projector and stores the images. The program was written in C++ in cooperation with Jan Tusch with the Fox tool kit library (for the graphical user interface) and was about 6000 lines long. The computer (a Pentium 4 PC) was running under the Windows operating system.

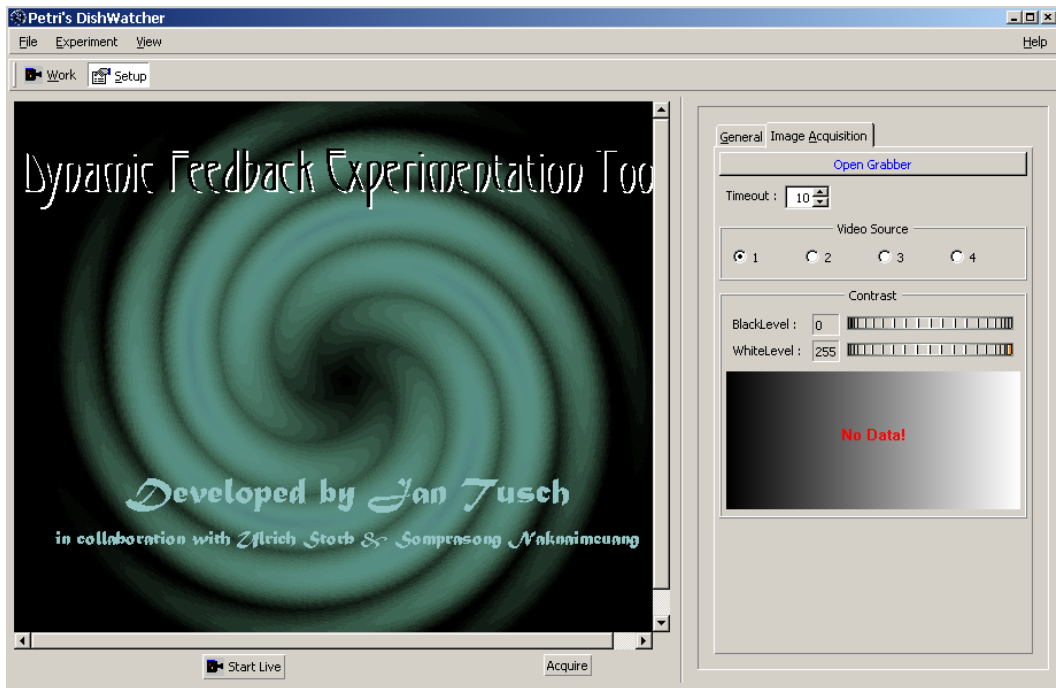


Figure 2.4: Initial GUI of controlling program.

The controlling program starts by creating a graphical user interface (GUI) which allows the user to view the current image from the CCD camera and enter the parameters (as shown in Figure 2.4). When the program starts, a window appears and the user presses the *open frame grabber* button. The image, which is then updated every 10 ms appears on the left-hand side of the window as shown in Figure 2.5. The user then chooses which type of integration area by pressing the appropriate button. The choices available are rectangle, triangle, pentagon, ellipse or annulus. The user then uses the mouse to click on the image to specify the size and position of the integration area. The values of I_0 (background intensity), B_0 (average grey level of each pixel inside the integration area when the tip of the spiral wave is in the centre) and k_{fb} (feedback gain) are entered by using spin boxes on the right-hand window.

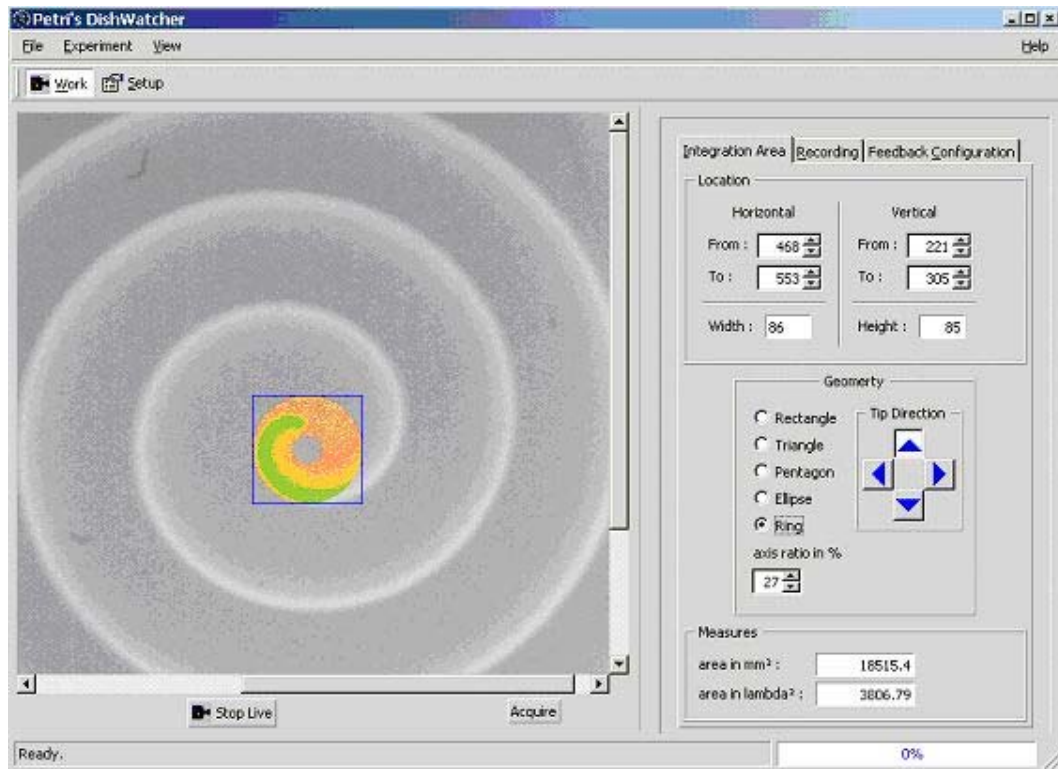


Figure 2.5: Specifying the integration area.

In the final stage of setting up, the user specifies the rectangular recording area by clicking on the image and choosing the time interval between recording the images. Then the user presses the *start* button and a window is created for displaying the value of the feedback illumination, the maximum number of recorded images (after which the program stops), and the time as shown in Figure 2.6. The program then enters the main loop.

Inside the main loop, the program sends a signal to the projector to set the intensity to I_0 . The program gets the image data from the frame grabber and calculates the average grey level of each pixel inside the integration area. Then the program calculates the feedback illumination I and changes the projector illumination accordingly. Each measurement cycle lasts 1.5 s. During the first 0.1 s the CCD image is acquired and the value of I is calculated while the dish is illuminated with intensity I_0 . For the remaining 1.4 s, the dish is illuminated with intensity I , and the image is stored as a TIFF file. The main loop is repeated until the user presses the *stop* button.

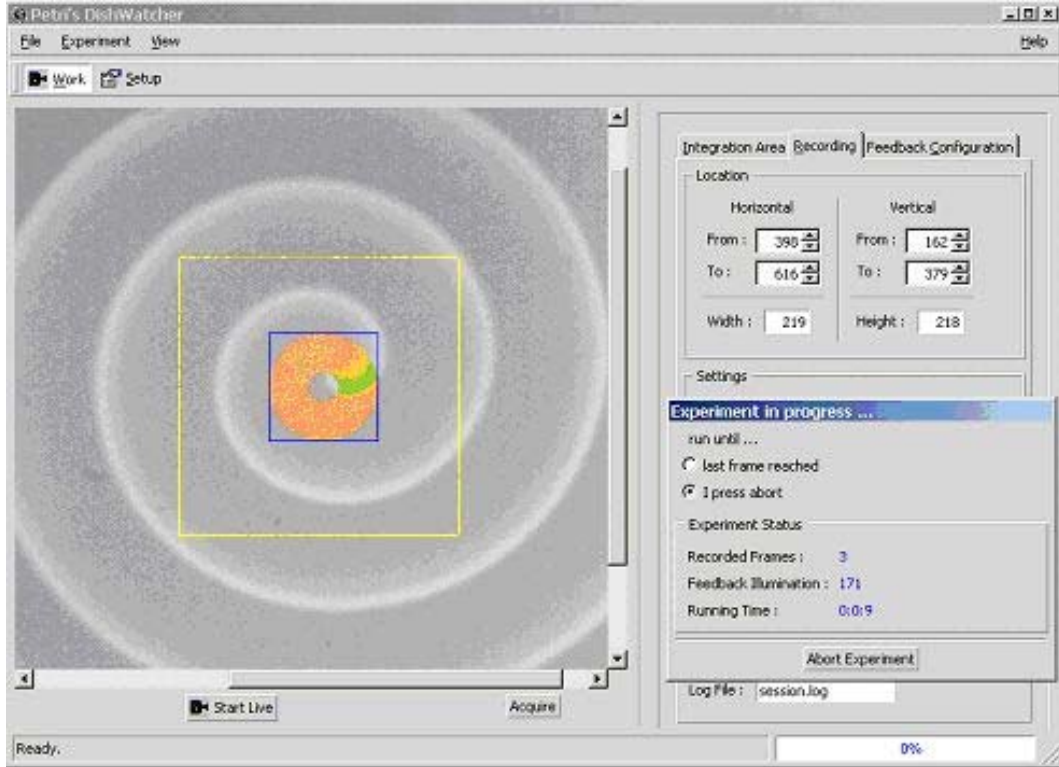


Figure 2.6: Appearance of GUI while gathering data.

2.5 Obtaining the control parameters

The background intensity, I_0 is chosen so that the spiral wave does not meander. This value can vary from 0.8 to 1.2 W/m² but is typically 1.0 W/m². To determine the value of I_0 for a rigidly rotating spiral wave, first a constant illumination of 0.8 W/m² is applied. Then if the core is meandering a little, the intensity is increased gradually until rigid rotation is obtained. However, if the core is meandering considerably, no value of I_0 can be found to give rigid rotation and the experiment cannot be continued.

If k_{fb} is too small, the spiral core drift is very slow and the core will not travel far enough before the experiment has to be finished due to aging. On the other hand, if k_{fb} is too large, the approximation that the spiral wave rotation is fast compared to the core drift can no longer be made. The optimum value of k_{fb} was found to be given by $0.12 \text{ W m}^{-2} / \max(|B(t) - B_0|)$.

2.6 Image analysis

The image are processed and analysed using IDL programs written by Dirk Michael Goldschmidt and Vladimir Zykov. The data acquisition program stores the image as arrays of grey levels. These grey level values are in the range 150 to 180. The program `contrast.pro` maximizes the contrast of the images by rescaling the grey levels range from 0 to 255 by applying the following formula to each pixel:

$$I'_{ij} = 255 \frac{(I_{ij} - I_{min})}{(I_{max} - I_{min})} \quad (2.2)$$

where I_{ij} and I'_{ij} are the original and rescaled grey levels of pixel (i, j) , and I_{max} and I_{min} are the maximum and minimum values in the original image. The image contains a background of inhomogeneities due to impurities in the gel such as bubbles, dust and scratches on the Petri dish. This can be corrected by a histogram method [58]. The background is then subtracted from the normalized image and the image normalized again using (2.2) and stored as new files to be read by `tipfinder.pro`.

The program `tipfinder.pro` finds the position of the tip by obtaining the contour lines for the grey level $0.6(I_{max} - I_{min}) + I_{min}$. The intersection of these contour lines for consecutive images gives the position of the tip [58].

Chapter 3

Numerical Calculation

3.1 Numerical solution of excitable system equations

The excitable system we study numerically is governed by the equations

$$\frac{\partial u}{\partial t} = D_u \nabla^2 u + F(u, v) - I(t), \quad \frac{\partial v}{\partial t} = \varepsilon G(u, v) \quad (3.1)$$

where u and v are the concentrations of activator and inhibitor, respectively. For the reaction terms $F(u, v)$ and $G(u, v)$ we chose to use Zykov's piecewise linear model as it is straightforward to obtain a rigidly rotating spiral using this [37]. It is possible to obtain rigid rotation using other excitable system models, but this requires fine tuning of the parameters. The piecewise linear model we use has the additional advantage that the reaction terms are simpler to evaluate than other schemes and so the code runs faster. The functions take the form

$$F(u, v) = f(u) - v, \quad f(u) = \begin{cases} -k_1 u, & u \leq \sigma, \\ k_f(u - a), & \sigma \leq u \leq 1 - \sigma, \\ k_2(1 - u), & 1 - \sigma \leq u, \end{cases} \quad (3.2)$$

$$G(u, v) = \begin{cases} k_g u - v, & k_g u - v \geq 0, \\ k_\varepsilon(k_g u - v), & k_g u - v \leq 0. \end{cases} \quad (3.3)$$

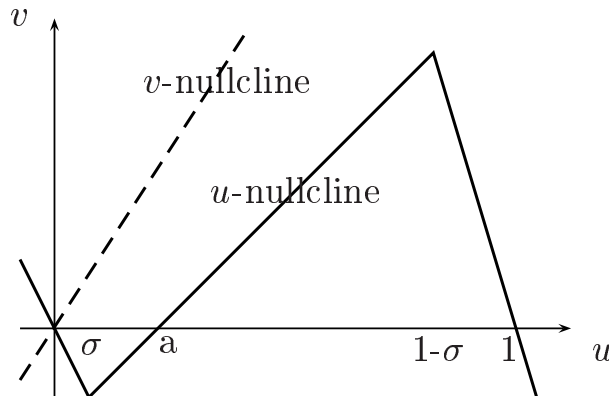


Figure 3.1: Sketch of u -nullcline ($v = f(u)$) and v -nullcline ($v = k_g u$) for Zykov's piecewise linear excitable system model (3.2 and 3.3).

As in Ref. [37], we used the following parameter values: $k_f = 1.7$, $k_g = 2$, $k_\varepsilon = 6.0$, $a = 0.1$, $\sigma = 0.01$, $\varepsilon = 0.3$ and $D_u = 1$. Parameters k_1 and k_2 , which are chosen so that $f(u)$ is continuous, are then found to be 15.3 and 151.3, respectively. A sketch of the u - and v -nullclines is shown in Figure 3.1. The feedback term $I(t)$ is given by

$$I(t) = k_{fb}(B(t) - B_0), \quad B(t) = \frac{1}{S} \int_D v(x, y, t) dx dy \quad (3.4)$$

where S is the area of the sensory domain D over which the integration of v is performed, and B_0 is the average value of $B(t)$ over one revolution of a spiral wave located at the centre of the domain. Typically, the feedback gain, k_{fb} was given the value 0.1.

The numerical calculation was carried out using an adapted version of Barkley's program `ezspiral` [20]. The code integrates (3.1) using the explicit Euler method with a 9-point Laplacian and no-flux boundary conditions, and also determines the location of the spiral tip. A time step of 0.05 and a space step of 0.5 were used throughout. A rigidly rotating spiral of pitch 70 space units that rotates about a core of radius 7 units is obtained by using the following initial conditions [37]:

$$u(r, \theta) = \begin{cases} 1, & r > 2 \text{ and } 0 \leq \theta < \pi/4, \\ 0, & \text{otherwise,} \end{cases}$$

$$v(r, \theta) = \begin{cases} 2, & r \leq 2, \\ 1.6 - 5.2\theta/\pi, & r > 2 \text{ and } 0 \leq \theta < \pi/4, \\ 0.3 + 5.2(\theta - \pi/4)/(7\pi) & r > 2 \text{ and } \pi/4 \leq \theta < 2\pi. \end{cases}$$

The discrepancy between the value of the pitch we obtain and that given in Refs. [40, 39] of 64 in spite of our using identical parameter values is due to the fact that we used a larger time step and the 9-point rather than 5-point Laplacian. With time steps of less than 0.2 and 0.05, the 9 and 5-point calculations give pitches of 66 and 64, respectively. After normalizing the length to be in units of spiral wavelength the plots obtained from using the larger and smaller time steps were found to be essentially the same.

3.2 Drift vector field

To aid interpretation of the experimental and numerical results, we also plot the drift vector field which depicts the drift velocity of the spiral core [39]. The vector plot analysis shows the direction of the spiral wave movement in any position both inside and outside the sensory domain. By following the arrows one can determine the trajectory of the the spiral tip.

As long as k_{fb} is not too large, the spiral core does not move far during one rotation of the spiral wave. The feedback term $I(t)$ that appears in (3.4) may therefore be approximated as being periodic (with a period equal to T_∞) and hence may be expressed as the Fourier series

$$I(t) = k_{fb} \left[\frac{a_0}{2} + \sum_{n=1}^{\infty} (a_n \cos n\omega t + b_n \sin n\omega t) \right] \quad (3.5)$$

where $\omega = 2\pi/T_\infty$. It has been shown that a systematic (resonant) drift of the spiral core will only occur if

$$\omega = p\omega_2 + q\omega_f \quad (3.6)$$

where ω_2 is the secondary (meandering) frequency, ω_f is the forcing frequency, and p and q are integers [29]. For rigid rotation, $\omega_2 = 0$ and from (3.5) it

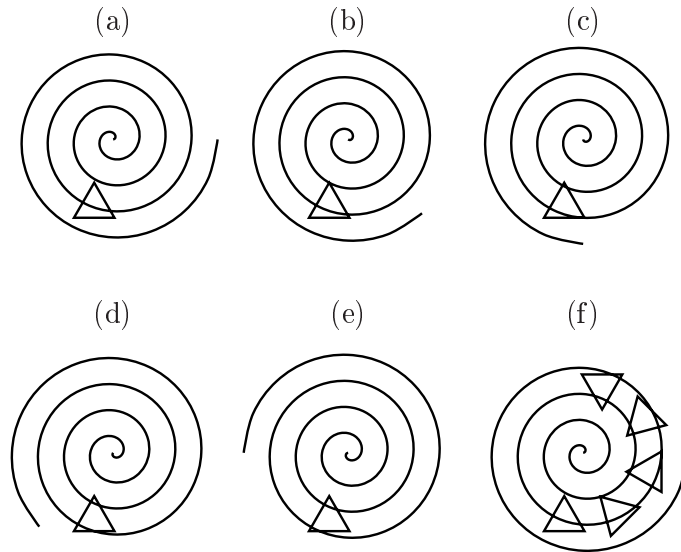


Figure 3.2: Illustration of the method for calculating $B(t)$. Rotation of the spiral wave with a fixed domain (a-e) is equivalent to rotating the domain with a fixed spiral wave (f).

can be seen that the forcing frequencies are $\omega_f = n\omega$. Hence (3.6) will only be satisfied if $n = q = 1$ which means that only the first Fourier component (a_1, b_1) results in spiral core drift [39]. The relative magnitude of the drift velocity is therefore given by the amplitude of the first Fourier component of $B(t)$. The direction of the velocity is equal to $\phi + \phi_0$ where ϕ is the phase of the first Fourier component and ϕ_0 is a constant. ϕ_0 can be obtained for a single vector in the plot by first carrying out a simulation starting at the position of that vector. Comparing the direction of the spiral core drift from the simulation with the ϕ obtained from the first Fourier component will give the required value of ϕ_0 .

In Ref. [39] the $B(t)$ needed for the drift vector plot was found by approximating the wavefront as a thin Archimedean spiral. Instead, we first used the program to obtain a fully formed spiral wave which was then stored for later retrieval. To find the value of $B(t)$ over one period of rotation, creating a new array containing data for a translated and rotated spiral wave from the initial spiral wave data would be very time consuming. Hence rather than keeping the domain fixed and rotating the spiral in this way (see Figure 3.2(a-e)), it is much more efficient to instead translate and rotate the domain relative to the fixed spiral wave data as illustrated in Fig 3.2(f).

In the case of an equilateral triangular domain, the 3-fold rotational symmetry about the triangle centroid was exploited by evaluating the drift vectors on a triangular grid centred on this point for values of the polar angle in the range $0 \leq \theta < 120^\circ$. These vectors could then be used to obtain the remaining drift vectors in the regions $120^\circ \leq \theta < 240^\circ$ and $240^\circ \leq \theta < 360^\circ$ by rotating the vectors by 120° and 240° , respectively. For all other types of sensory domain, the drift vectors were evaluated on an ordinary rectangular grid.

3.3 Divergence plot

The drift vector fields obtained for larger domain sizes are quite complex. Visualization of the flows and attractors is greatly enhanced by colouring the arrows and background according to the sign of the divergence since attractors and repellers will occur in regions of negative and positive divergence, respectively. We use a normalized divergence obtained by dividing the divergence by the mean magnitude of the vectors used to calculate the divergence. For a rectangular grid, the normalized divergence $\mathcal{D}_{i,j}$ at point (i, j) is given by

$$\mathcal{D}_{i,j} = \frac{F_x^+ - F_x^- + F_y^+ - F_y^-}{|F_x^+| + |F_x^-| + |F_y^+| + |F_y^-|}$$

where

$$F_x^\pm = A_{i\pm 1,j} \cos \Phi_{i\pm 1,j}, \quad F_y^\pm = A_{i,j\pm 1} \sin \Phi_{i,j\pm 1},$$

in which $A_{i,j}$ is the amplitude of the drift vector at (i, j) and $\Phi_{i,j} = \phi_{i,j} + \phi_0$. For a triangular grid,

$$\mathcal{D}_{i,j} = \frac{F_0^+ - F_0^- + F_1^+ - F_1^- + F_2^+ - F_2^-}{|F_0^+| - |F_0^-| + |F_1^+| - |F_1^-| + |F_2^+| - |F_2^-|}$$

where

$$F_0^\pm = A_{i\pm 1,j} \cos \Phi_{i\pm 1,j}, \quad F_1^\pm = A_{i\pm 1,j\pm 1} \cos(\Phi_{i\pm 1,j\pm 1} - \pi/3),$$

$$F_2^\pm = A_{i,j\pm 1} \cos(\Phi_{i,j\pm 1} - 2\pi/3).$$

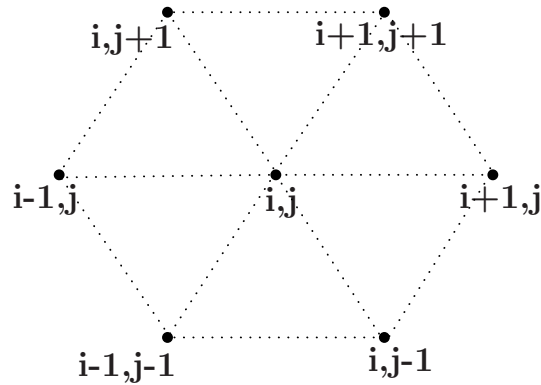


Figure 3.3: Location of points in triangular grid. The connection lines are guideline for the eyes

For the triangular grid the relative positions of the grid points are illustrated in Fig 3.3. The origin of the triangular grid ($i = 0, j = 0$) is at the centroid of the equilateral triangular domain. The remainder of the coordinates on the lattice are defined in such a way that moving in the $\theta = 0$ direction i increases while j remains fixed. Moving in the $\theta = 120^\circ$ direction, j increases while i remains fixed.

Colouring the arrows and background in this way shows regions where the magnitude of the vectors is low particularly striking. A very dark background indicates that the vectors are small and are converging. A very bright background shows that the vectors are small and are diverging. Some examples are shown in Figure 3.4.

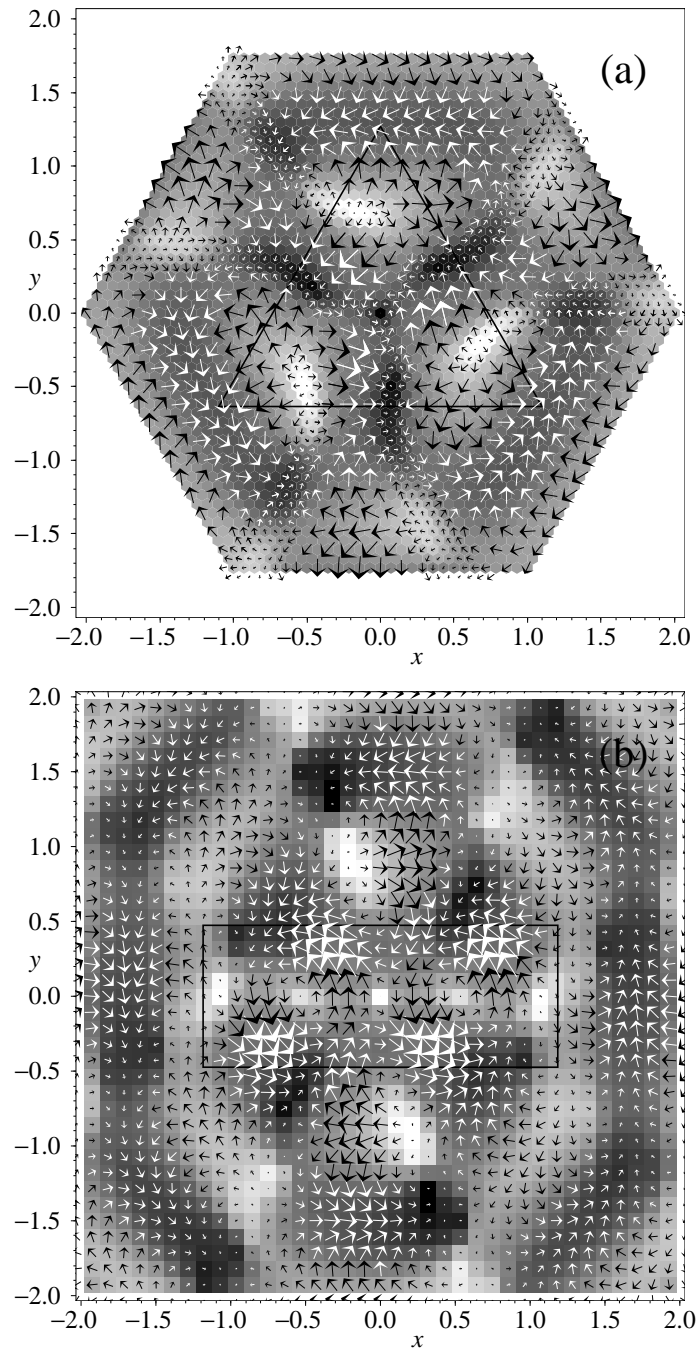


Figure 3.4: Drift vector plots coloured according to the normalized divergence.(a) for triangle grid and (b) for rectangle grid.

Chapter 4

Plane Wave Approximation

In this chapter we describe a straightforward technique that can be used to account for some features of the behaviour of the core trajectory when it is far from the domain. To explain features of the drift vector fields, we would ideally require an analytical expression for the feedback integral $B(t)$. In the Archimedean spiral wave approximation, $B(t)$ is calculated by finding the total length of the sections of an Archimedean spiral that lie inside the domain [39]. In general, such an expression cannot be written in closed form. However, since the curvature of a spiral wave decreases with increasing distance from the core, for sufficiently large core-domain distances we can treat the parts of the spiral wave inside the domain as a series of plane waves with a wavelength equal to that of the spiral wavelength far from the core. In the following, for simplicity we scale the spatial coordinates so that this wavelength is equal to 1. The plane waves will be propagating away from the spiral core in the direction of the centre of the domain as illustrated in Fig. 4.1(a). As the tip rotates about the core (which is taken to have zero radius) once in time T_∞ , the plane wavefronts move forward one unit at uniform speed. In this plane wave approximation (PWA) the feedback integral $B(t)$ is given by the sum of the lengths of the lines inside the domain divided by the domain area.

The PWA is most useful when the domain is in the shape of a polygon. It is apparent that in this case, $B(t)$ will increase or decrease linearly and hence $B(t)$ will take the form of a piecewise linear function of period T . If the plane wave is parallel to one of the sides, there will be a discontinuous change in $B(t)$ as the wavefront crosses one of the sides. The change will be an increase

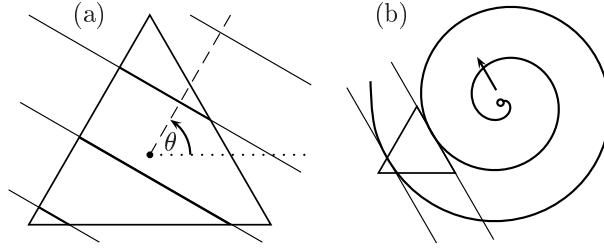


Figure 4.1: Plane wave approximation. In (a) spiral core is in the direction of the dashed line. In (b) the small circle represents the spiral core and the arrow the current direction of motion of the tip.

if the wavefront is entering the domain side and a decrease if it is leaving it. For example, in Fig. 4.1(a) if $\theta = 90^\circ$, the plane wavefronts enter the domain at a vertex. The total length of the plane waves inside the domain will steadily increase until a plane leaves the domain at the side opposite the vertex where they enter. At this point $B(t)$ will suddenly drop. Overall, $B(t)$ will take the form of a rising sawtooth wave. Conversely, if $\theta = 30^\circ$, it can be seen that $B(t)$ will take the form of a falling sawtooth wave.

Now consider the case when the spiral core is a half integer number of wavelengths from one of the sides. As the spiral wave (approximated by a plane wave) crosses the side of the triangle, there will be a sudden increase in the excitability resulting in a boost to the motion of the tip and hence also the core in the direction shown. Now consider moving the spiral core a little further away from the domain. In order for the wavefront to touch the side, the spiral must be rotated anticlockwise. Thus as the spiral core moves away from the domain, the drift velocity vectors rotate anticlockwise, completing one rotation every wavelength. From this one can conclude two points. First, the spiral core shown is therefore in the centre of an attracting region. Second, these attracting regions will be spaced at an interval of one unit. We would therefore expect to see attracting (repelling) limit cycles to be spaced 1 unit apart in regions far from the domain.

It is evident that the greatest difference between the maximum and minimum values of $B(t)$ will occur when the plane waves are aligned with a side, as in the examples mentioned earlier. The Fourier components of $B(t)$ will be proportional to this difference in values. Since the drift velocity is proportional to the magnitude of the first Fourier component, the drift velocity will be the

largest in these cases.

The drift vector plots obtained in this work and by others [39, 40] show a number of striking features in the regions far from the domain. In particular, it is clear that there are regions where the drift velocity is either particularly large or almost zero. The PWA developed here gives a relatively straightforward approach to account for these features. Further details of this method are given in the following chapter where it is applied to some specific cases.

Chapter 5

Experimental and Numerical Results

The effect of feedback on spiral wave trajectories is studied using two different shapes of sensory domain. The simpler of our systematic studies is for the equilateral triangle, since this geometry only has one parameter to vary, namely, the domain size. The isosceles triangular domain has two parameters. Some of the results can be explained using the plane wave approximation described in the previous chapter.

The experimental studies were carried out with anticlockwise spiral waves (which appear to rotate clockwise as the wavefront propagates). The image from the IDL program was inverted due to programming technique and so the anticlockwise spirals used in the experiment appeared as clockwise spirals. For ease of comparison, the numerical computations were therefore also performed using clockwise spirals. The plots for anticlockwise spiral waves would be a mirror image of the ones presented here.

5.1 Equilateral triangular domain

First, spiral wave dynamics under feedback via an equilateral triangular sensory domain is considered. The domain size, d , is defined as the length of a side of the triangle. From now on, all lengths are given in units of the spiral wavelength, λ_∞ .

The experimental results for an equilateral triangle domain show a number

of types of behaviour. The behaviour depends on the size of the domain. When the length of the domain d is less than about 1.3, after feedback illumination is applied to the system, the spiral tip moves out of the domain and drifts around the domain in an approximately circular path and then repeats this orbit as we can see in the experimental and numerical results of Fig. 5.1. The attractor is therefore a stable limit cycle with an approximately circular shape. The result is similar to the results found for a square domain. When the length of the square domain is smaller than 1 the spiral tip drift around the square domain is also in a circular path [49]. The numerical results show further that the central source is surrounded by concentric alternately stable and unstable limit cycles.

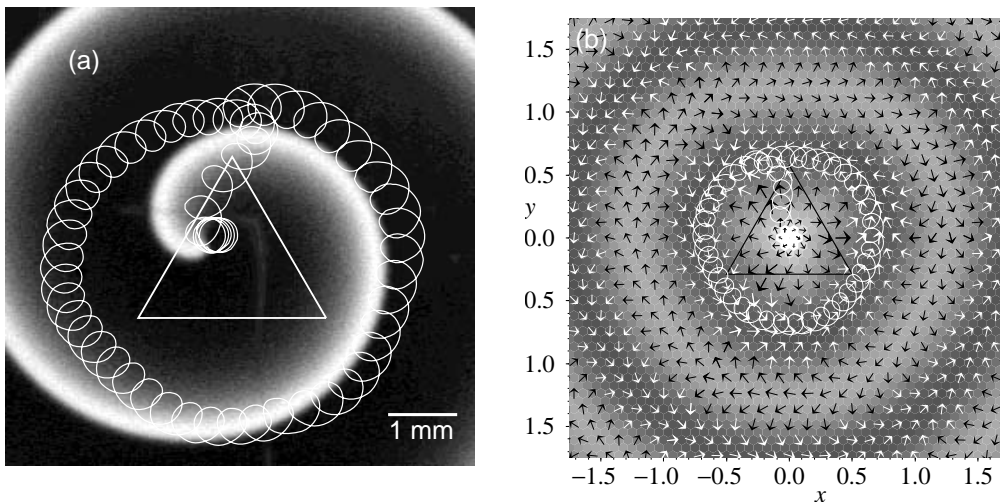


Figure 5.1: (a) Experimental results for the spiral wave tip drift in circular path with equilateral triangular domain $d = 1$. In this and later plots obtained from experiments, the spiral wave image is taken at the start of the tip trajectory. Feedback is initiated after a few revolutions of the tip. (b) Numerically obtained drift vector plot for $d = 1$. In this and subsequent plots of this type, the black triangle is the domain, the white curves are the spiral tip paths, and the arrows indicate the drift velocity. The length of all but the small, narrow-headed arrows is proportional to the drift speed (although the proportionality constant differs for each plot). Black (white) arrows are in regions where the field divergence is positive (negative). The background is shaded according to the normalized divergence (see section 3.3). Regions of negative (positive) divergence have a dark (light) background.

For some larger values of d , the attractor has the shape of an equilateral triangle as shown in the experimental results of Fig. 5.2 and numerical results

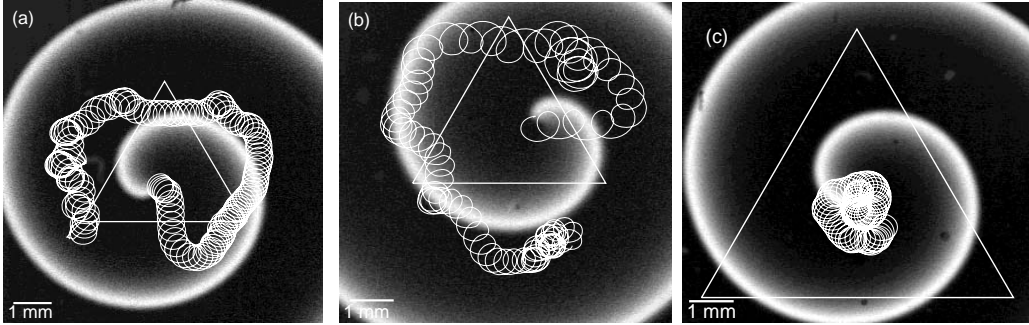


Figure 5.2: Experimental results showing triangular limit cycle for various values of (d, k_{fb}) : (a) (1.3, 0.6); (b) (1.5, 0.6); (c) (2.3, 1.0).

in Fig. 5.4(a). This attractor is in the opposite orientation compared with the domain. For d between 1.3 and 1.5, the attractor is approximately the same size as the domain. For larger d , the size of the attractor decreases as d increases. In all instances, the stable limit cycles flow anticlockwise, while the unstable limit cycles are in the opposite sense. Starting close to an unstable limit cycle, the spiral core first drifts clockwise and then reverses its sense as it approaches a limit cycle as can be seen in Fig. 5.5(a).

By around $d = 1.5$, it is clear from the computational results that there are regions where the spiral core speed is large (long arrows) and those where it is small (short arrows), aside from near the single fixed point at the centroid (Fig. 5.4(a)). We refer to these as express and stagnation zones, respectively. As with the regions in the immediate neighbourhood of sinks (stable nodes/foci) and sources (unstable nodes/foci), the stagnation zones appear as the darkest or brightest regions of the plot depending, respectively, on whether the divergence is negative or positive (see section 3.3). Notice in Fig. 5.4(a) that the innermost limit cycle passes through three stagnation zones (the spiral core move slowly). It will be convenient to classify the express zones according to the direction from the centroid in which they lie and whether they are attracting (white arrows) or repelling (black arrows). Vertex express zones (VEZs) lie in the directions of the domain vertices, namely, $\theta = -30^\circ, 90^\circ, -150^\circ$, whereas lateral express zones (LEZs) are located in the opposing directions away from the centroid (Fig 5.3).

Just outside the domain is an approximately hexagonal unstable limit cycle

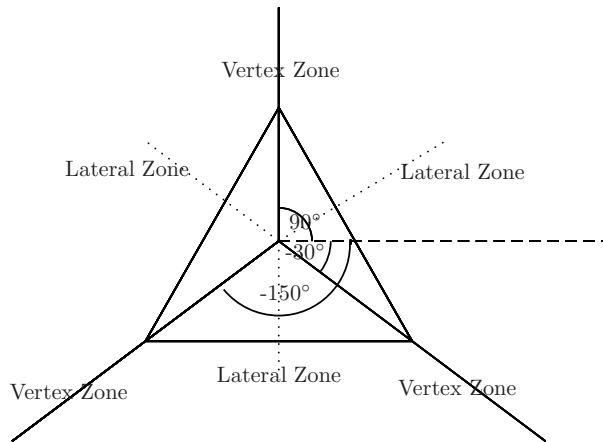


Figure 5.3: Sketch of the region where vertex and lateral zone are indicated for the triangular domain. VEZs and LEZs are the region where the large magnitude arrows take place in the vertex zone and lateral zone, respectively.

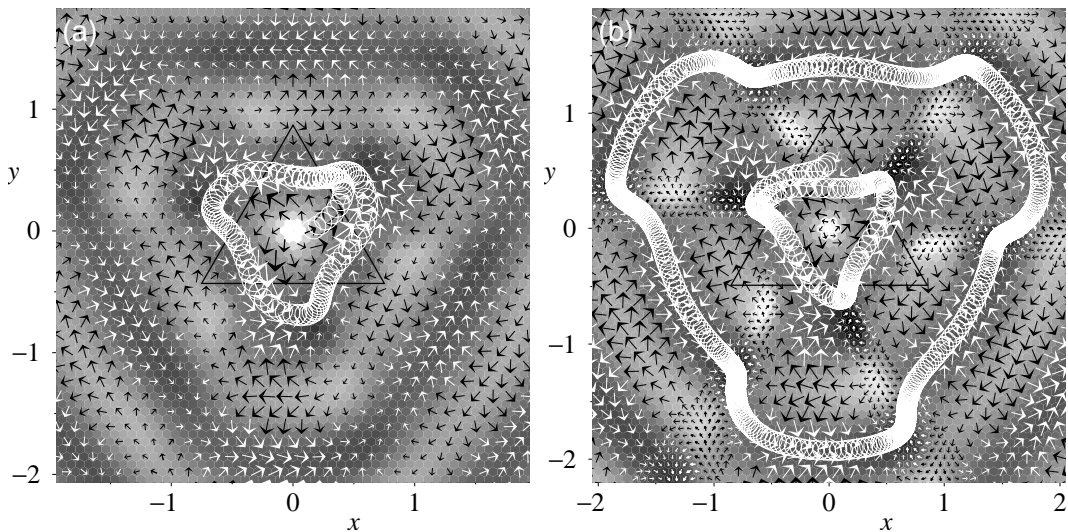


Figure 5.4: Drift vector plots. (a) $d = 1.5$. The tip trajectory starts near the central unstable focus and ends up on the innermost stable limit cycle. (b) $d = 1.7$ - tip trajectories shown following the first two stable limit cycles.

lying within six repelling express zones (3 LEZs and 3 VEZs) interspersed with six weak stagnation zones. Further out there is a stable limit cycle of similar shape lying within six attracting express zones.

As d increases further, the distance from the centroid to the VEZs decreases, while the corresponding distance to the LEZs increases. This results in the second stable limit cycle having three protruding lobes as can be seen in Fig. 5.4(b). We will refer to such lobed limit cycles as being of lateral or

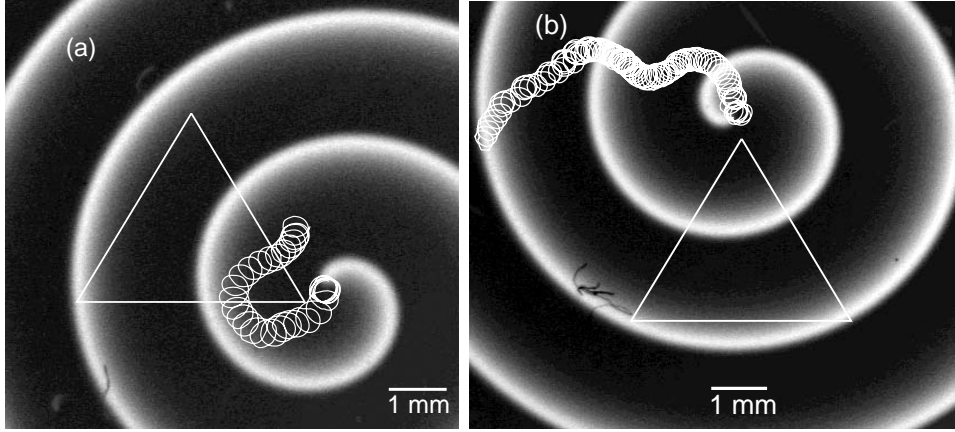


Figure 5.5: Experimental results for $d = 1.8$: (a) Spiral core trajectory starting at the right bottom vertex, it reaches the inner limit cycle ($k_{fb} = 0.6$); (b) Spiral core trajectory entering lobed limit cycle ($k_{fb} = 1.4$).

vertex type depending on whether the most protruding parts (the ‘lobes’) are composed of LEZs or VEZs, respectively. Part of a lateral lobed limit cycle is clearly seen in the experimental results shown in Fig. 5.5(b). Notice the presence of the stagnation zone (where the loops are bunched together) at the start of the lobe.

As a result of the increase in separation of the ends of the LEZs from the ends of the VEZs, the limit cycles become ever more distorted until just below $d = 1.82$ in the computational results both the innermost unstable limit cycle and the lobed stable limit cycle surrounding it are destroyed via saddle-node bifurcations. With the two limit cycles destroyed, the basin of attraction for the central stable limit cycle becomes much larger – trajectories starting on and around the express zones that contained part of the destroyed lobed limit cycle will eventually make their way to it via a number of (negative divergence) stagnation zones. However, this extended basin is short-lived. By $d = 1.85$, a further saddle-node bifurcation results in each of the innermost LEZs no longer connecting with the central limit cycle. Instead they link with the next attracting VEZs to form a vertex lobed stable limit cycle, as can be seen in Fig. 5.6. A further (lateral) lobed stable limit cycle passes through the second set of attracting VEZs. Trajectories starting on the attracting VEZs

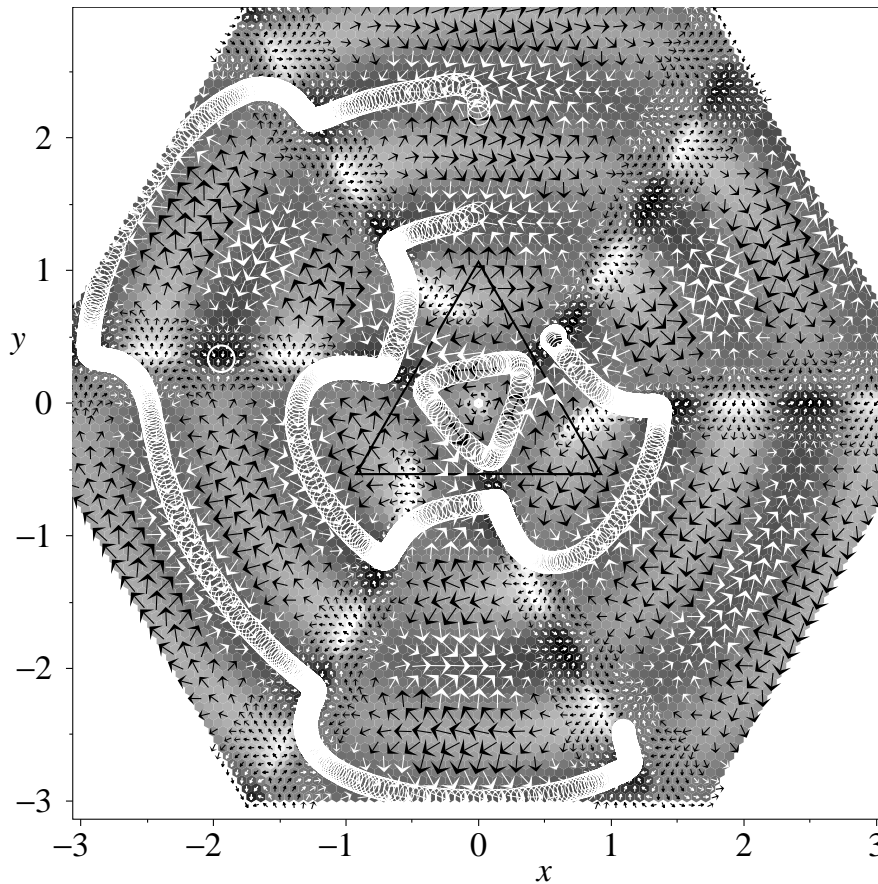


Figure 5.6: Drift velocity plot for $d = 1.85$. Tip trajectories follow (parts of) the first three stable limit cycles. The first limit cycle is inside the domain and has a shape of triangular path. The second and third are examples vertex and lateral lobed limit cycles, respectively. The isolated circle marks the position of a stable focus.

in between the second and third stable limit cycles will end in a sink. These sinks occur for only a small range of d . At $d = 1.86$ this second set of VEZs are part of the basin of attraction for the third limit cycle, and by $d = 1.90$, these VEZs make up part of the third stable limit cycle which is now vertex lobed.

The central stable limit cycle shrinks down to a stable focus (via a supercritical Hopf bifurcation) for $d \approx 2$ in the computational results, and at a value of d between 2.3 and 2.5 in the experiment (a small triangular limit cycle and sink at the centroid are shown in Fig. 5.2(c) and Fig. 5.7(a), respectively). The parts of the innermost vertex lobed limit cycle get ever closer to the centroid

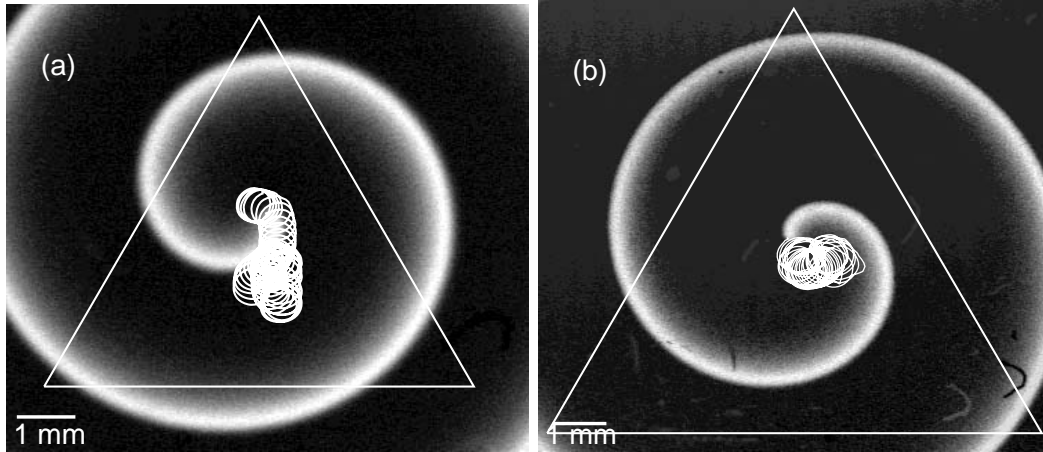


Figure 5.7: Experimental results showing the presence of a sink at the centroid for various (d, k_{fb}) : (a) $(2.5, 0.9)$; (b) $(3.0, 1.0)$.

as d increases. They are separated from the stable focus there by saddle nodes. At around $d = 2.6$ these saddle nodes move to one side with the result that the limit cycle is destroyed – trajectories starting on the first VEZs end up at the centroid. As before, the extended basin of attraction for the central attractor only occurs for a narrow range of domain size. By $d = 2.7$, trajectories starting on the first VEZ instead end up on a sink in the neighbouring stagnation zone Fig 5.8.

Having reached a domain size where there are no longer any limit cycles in the domain, it is of interest to survey the fixed points present. Referring to the region $0 \leq \theta < 120^\circ$ in Fig. 5.8, as well as the sinks at the centroid and in the stagnation zone, there is also a stable focus just inside the domain at $(0.62, 0.41)$ and further out a saddle node at $(0.96, 0.64)$. This pair of fixed points was born in a bifurcation inside a stagnation zone at around $d = 2.57$. Finally there is an unstable node at $(-0.07, 0.67)$ which first appeared when the first unstable limit cycle broke around $d = 1.82$. This lattice of evenly separated sources and sinks is reminiscent of the cellular structure seen for the square domain [39, 48]. As in that case, more fixed points appear inside the domain as the domain size is increased still further.

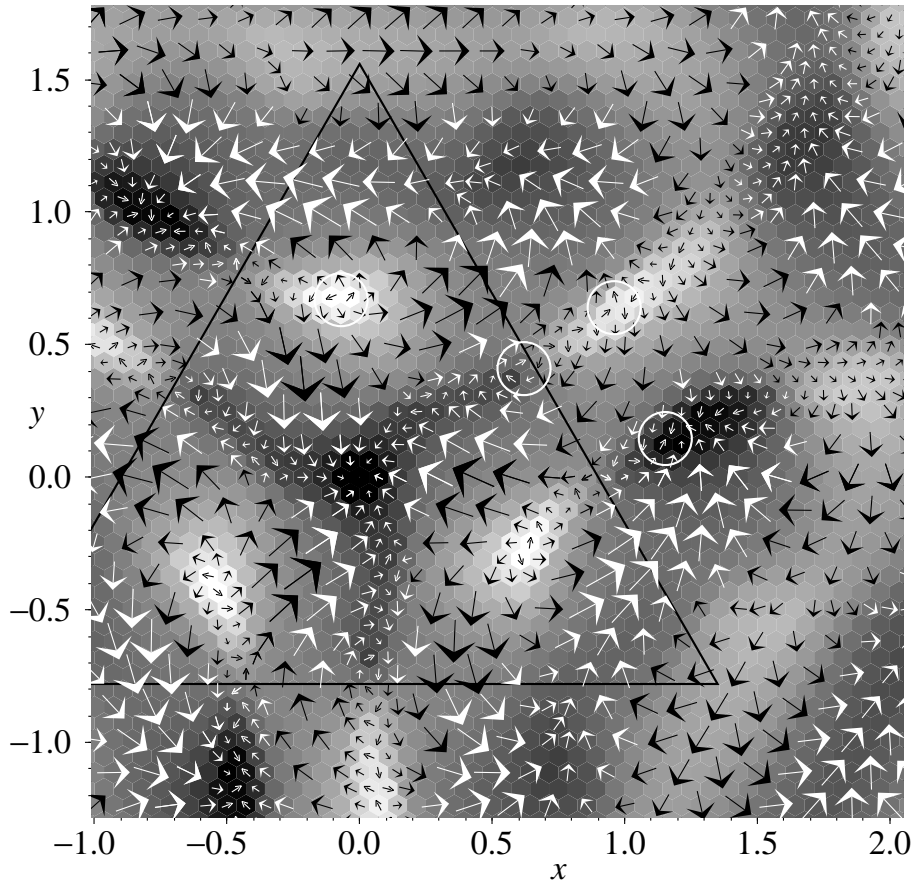


Figure 5.8: Drift velocity plot for $d = 2.70$. Selected fixed points referred to in the text are inside white circles.

Analysis using the plane wave approximation

We now turn our attention to the motion of the core when it is far from the domain and analyse it by means of the plane wave approximation (PWA) introduced in Chapter 4. As has been pointed out, since we are approximating the wavefront as a series of plane waves, it is relatively straightforward to obtain an explicit expression for $B(t)$. To do this we find the length $L(p)$ of the plane waves inside the domain as a function of p by first making the construction as shown in Fig. 5.9. The quantity p is the distance from O to the nearest plane wave in the direction of the spiral core. It therefore lies in the range $0 \leq p < 1$ and decreases with time. If time is scaled so that $T_\infty = 1$ then

$$p = (1 - t + t_0) \bmod 1 \quad (5.1)$$

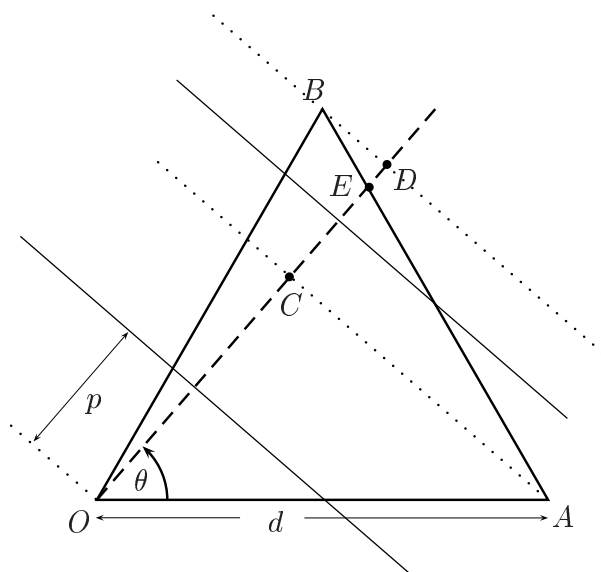


Figure 5.9: Construction used to find $L(p)$ for an equilateral triangular domain. The spiral core is in the direction of the dashed line. Solid lines perpendicular to the dashed line are wavefronts. They are one unit apart and move towards O .

where t_0 is a time at which a plane wave passes through O . We only need to consider the cases $30^\circ \leq \theta \leq 90^\circ$ since in addition to the 3-fold rotational symmetry, there is also reflection symmetry about the line $\theta = 30^\circ$. For $30^\circ < \theta < 90^\circ$, a wavefront passing inside the domain either intersects OB and OA or OB and AB . The number of wavefronts that intersect OB and OA is the number, M , of wavefronts that lie between O and C . Point C lies on the dashed line in such a position that AC is perpendicular to OC . Hence

$$M = [OC - p + 1] = [d \cos \theta - p + 1] \quad (5.2)$$

where $[\cdot]$ represents the integer part. The remaining wavefronts that pass through the domain and intersect OB and AB , lie between C and D . Point D lies on the dashed line in such a position that BD is perpendicular to OD . If N is the number of wavefronts between C and D then it can be found from the total number of wavefronts in the domain which is given by

$$M + N = [OD - p + 1] = [d \cos(60^\circ - \theta) - p + 1]. \quad (5.3)$$

To find $L(p)$ we need to introduce a further point E which is the intersection of the dashed line with the line that passes through A and B . Then using simple geometry we obtain

$$L(p) = \sum_{m=0}^{M-1} (p+m) \{\tan \theta + \tan(60^\circ - \theta)\} + \sum_{m=M}^{M+N-1} (p+m) \tan(60^\circ - \theta) + \{OE - (p+m)\} \tan(120^\circ - \theta) \quad (5.4)$$

where the length OE is given by

$$OE = d\{\cos \theta + \sin \theta \tan(\theta - 30^\circ)\}.$$

$B(t)$ is then obtained from (5.4) by substituting in (5.1) and then dividing the whole expression by the area of the triangle.

When $\theta = 30^\circ$, the plane wavefronts enter the domain parallel to side AB . Points C and D coincide and the right-hand sides of (5.2) and (5.3) are the same which means that $N = 0$ and

$$M(p) = \left[\frac{\sqrt{3}d}{2} - p + 1 \right]. \quad (5.5)$$

Expression (5.4) then becomes

$$L(p) = \frac{2}{\sqrt{3}} \left\{ M(p)p + \frac{1}{2}M(p)(M(p) - 1) \right\}. \quad (5.6)$$

It can be seen that if $d = 2n/\sqrt{3}$ where n is an integer, then (5.5) will evaluate to a single number for any $0 < p < 1$. (We can ignore the case when $p = 0$ since this is only a single point and will have no effect on the final result.) This corresponds to there being a constant number of wavefronts in the domain (except when $p = 0$). From (5.6) it can be seen that $L(p)$ increases uniformly with p and hence that $B(t)$ will be a sawtooth wave with negative gradient. The phase of the first Fourier component of $B(t)$ will then be $\pi/2$ behind the discontinuity of the wave. For other values of d , $M(p)$ can take on two values, depending on p . This results in $B(t)$ having two different negative gradients for

$d \geq 2/\sqrt{3}$. The phase of $B(t)$ is then not exactly $\pi/2$ behind the discontinuity of the wave, but close to this value.

Similarly, when $\theta = 90^\circ$, the plane wavefronts enter the domain at B parallel to side OA . Following through the analysis in a similar way, one finds that $B(t)$ takes the form of a positive gradient sawtooth wave when $d = 2n/\sqrt{3}$ for which the phase of the first Fourier component is $\pi/2$ ahead of the discontinuity in $B(t)$. For other values of d , the phase differs from this slightly.

We are now ready to account for the positions of the LEZs and VEZs. Referring back to Fig. 4.1(b), it is now apparent that the spiral core in the figure is at the centre of an attracting LEZ and that in general the LEZs are located at distances from the centroid of $m + \frac{1}{2} + d/\sqrt{12}$, where m is an integer. The net phase difference of approximately π between the two cases of $\theta = 30^\circ$ and $\theta = 90^\circ$ results in the centres of attracting VEZs occurring at integer, rather than half-integer, distances from the side and hence their distances from the centroid are $m - d/\sqrt{12}$. These expressions explain why LEZs move away from the centroid while VEZs move towards it with increasing d . One also sees that since the switching between vertex and lateral lobed limit cycles described earlier for the region near the domain for $1.8 < d < 1.9$ results from the opposing directions of motion of the VEZs and LEZs, this switching phenomenon is generic for this system and hence will also occur for domain sizes and distances from the centroid larger than this.

In Fig. 5.10 the PWA estimates for the positions of the express zones are compared with the measured values from the numerical calculation. As expected, the agreement is best far from the domain. Also, for a given distance the discrepancy is larger for LEZs than VEZs. This is because how well the plane wave approximates the spiral wave depends on the distance of the core to the side which will evidently be smaller for a LEZ than a VEZ for a given core-centroid distance.

The PWA can also be used to explain some features of the magnitudes of the drift vectors in the directions of the side mid-points and vertices. First, if the spiral core in the centre of a VEZ or LEZ is moved directly away from the centroid, according to the PWA it will only result in a phase change in $B(t)$. Hence the magnitude of the drift vector in these directions should be

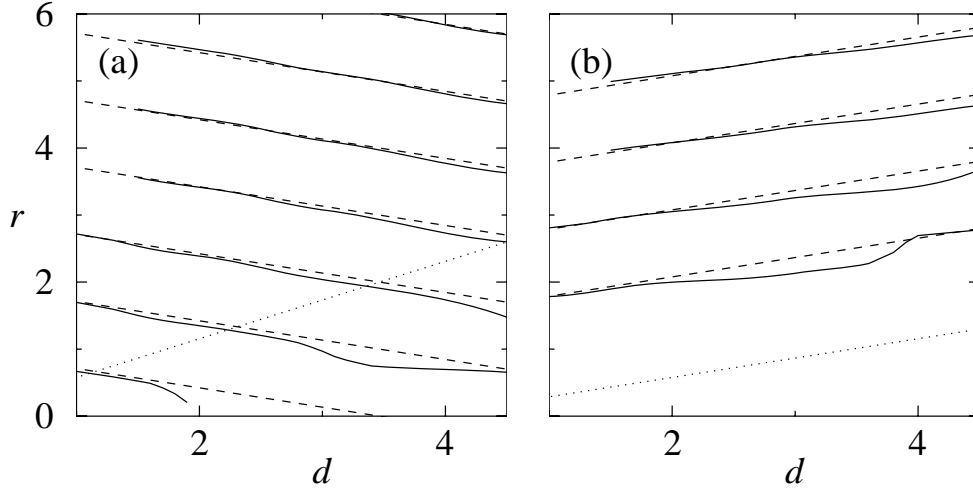


Figure 5.10: Distances of centres of attracting express zones in the directions of (a) the vertices (b) the mid-points of the sides. Solid lines: from computational results; dashed line: from PWA. The dotted lines show the edge of the domain.

constant. Note that this prediction is also true for the Archimedean spiral approximation. For the real spiral wave, which has a finite core radius, it would not be expected to be constant due to the tip not remaining in the same place as the wave rotates. Second, the difference between the maximum and minimum total length of the plane wavefronts in the domain is d . Since the area of the domain is proportional to d^2 , $B(t)$ and hence the drift velocity should be inversely proportional to d . As shown in Fig. 5.11, the measured range of drift vector amplitude, A , within an express zone is generally small. It is to be expected that this amplitude should be the same for VEZs and LEZs although this only appears to be the case near $d = 2$. The amplitudes certainly decrease with increasing d , but only approximately satisfy the inverse relationship obtained from the PWA.

We can also use the PWA to account for the occurrence, strength and positioning of the stagnation zones. When the plane waves are perpendicular to one of the sides, as is depicted in Fig. 4.1(a), the change in $B(t)$ and therefore magnitude of the drift velocity is minimized. If stagnation zones are present far from the domain, we therefore expect that they lie in the directions $\theta = n\pi/3$ away from the centroid. For plane waves traversing the domain in this way, it is easily seen that $B(t)$ will be constant (and hence the drift velocity zero)

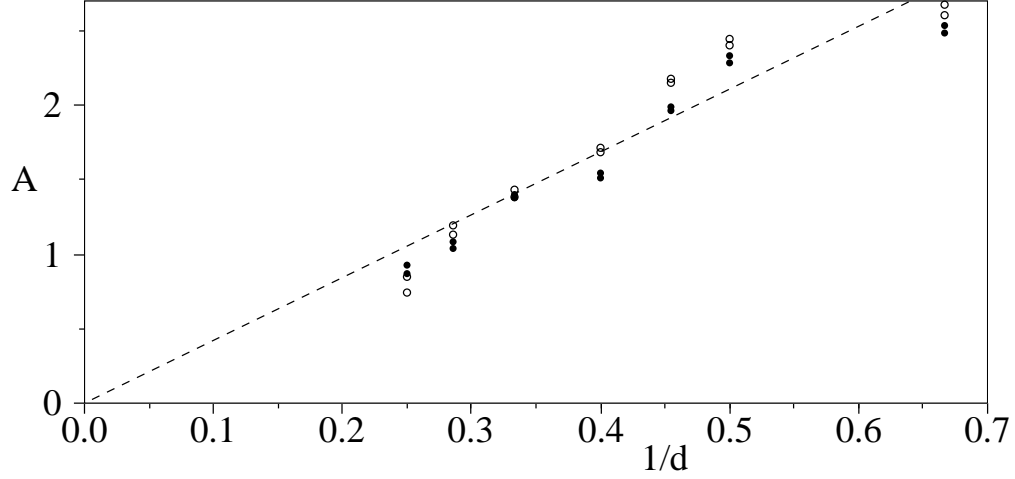
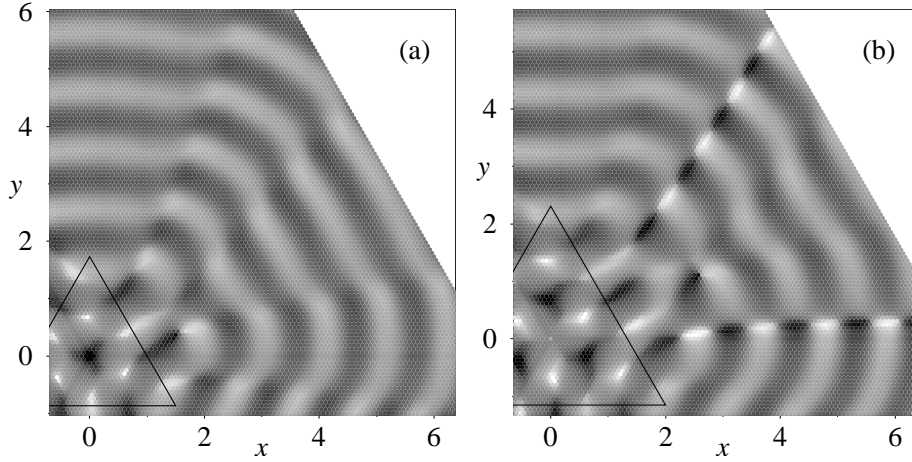


Figure 5.11: $(1/d, A)$ plot of maximum and minimum drift vector amplitudes lying in the directions $\theta = 30^\circ$ (open circles) and $\theta = 90^\circ$ (filled circles) for the express zones at a distance of about 6 from the centroid. The dotted line passes through the value with the smallest range of amplitudes.

if there are always an even number of wavefronts in the domain since for each wavefront whose length inside the domain is increasing, there will be a corresponding one whose length is decreasing by the same amount. As a result, according to the PWA it would be expected that the stagnation zones far from the domain should be strongest when d is close to an even integer. On the other hand, if there are always an odd number of wavefronts in the domain, $B(t)$ will vary with the result that the drift speed will not be very small. Hence for d close to an odd integer we expect very weak stagnation zones. This is seen for $d = 3$ in Fig. 5.12(a) in contrast to the very pronounced stagnation zones when d is close to an even integer as in Fig. 5.6 and Fig. 5.12(b). When $\theta = n\pi/3$, the PWA is at its crudest, and so the stagnation zones are only approximately in these directions.

There are another class of stagnation zones predicted by the PWA. If M and N are both constant then $L(p)$ will also be a constant as p varies. In the above case, $M = N$. However, if M and N are both any constant positive integers then we have

$$M = d \cos \theta \quad N = d \cos(60^\circ - \theta).$$

Figure 5.12: Normalized divergence plots for (a) $d = 3.0$ (b) $d = 4.0$.

Solving this gives

$$d = 2\sqrt{\frac{M^2 + N^2 + MN}{3}} \quad (5.7)$$

and

$$\cos \theta = \frac{M}{2} \sqrt{\frac{3}{M^2 + N^2 + MN}}. \quad (5.8)$$

Note that, as expected, when $M = N$, (5.7) reduces to $d = 2M$ and (5.8) reduces to $\cos \theta = \frac{1}{2}$ (i.e. $\theta = 60^\circ$). Putting $M = 2$ and $N = 1$ (or vice versa) in (5.7) gives $d = 2\sqrt{7/3} \simeq 3.055$, and from (5.8) one obtains $\theta = 49.1^\circ$ from $M = 2$, $N = 1$ and $\theta = 70.9^\circ$ from $M = 1$, $N = 2$. Reflection in the line $\theta = 30^\circ$ also gives the values $\theta = \pm 10.1^\circ$. As can be seen in Fig. 5.13, there is a pattern in the divergence plot in these directions. However, the stagnation zones are very weak. This is perhaps to be expected. In the idealization used in the PWA, the wavefronts are treated as infinitely thin lines. However, in the actual calculation of $B(t)$, the wavefronts have thickness. It is therefore unreasonable to assume that the decreasing of the extent of one wavefront in the domain could exactly compensate for the increasing of two wavefronts inside the domain on the other side of line AC . Note that these $(M, N) = (1, 2)$ and $(M, N) = (2, 1)$ type stagnation zones are also discernible in the plot for $d = 3$ shown in Fig. 5.12(a).

On the basis of the above argument, one would expect that the stagnation zones would be even weaker for the case $M = 3$, $N = 1$ (or vice versa). These values correspond to $d = 2\sqrt{13/3} \simeq 4.163$ and angles of

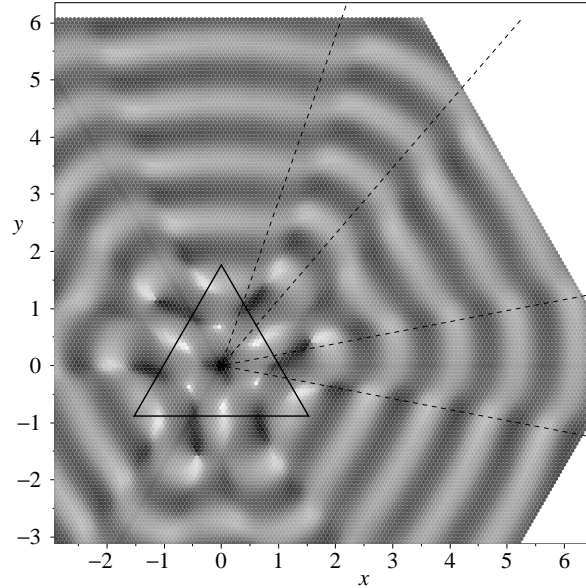


Figure 5.13: Normalized divergence plots for $d = 2\sqrt{7/3}$ showing the $(M, N) = (1, 2)$ and $(M, N) = (2, 1)$ stagnation zones. The dashed lines indicate angles at which the stagnation zones are predicted to lie by the PWA.

$\theta = 43.9^\circ, 76.1^\circ, \pm 16.1^\circ$. As can be seen in Fig. 5.14, this type of stagnation zone is scarcely existent. As in this case d is close to an even integer, the usual $d = 2M$ type stagnation zones are present in directions of $\theta = n\pi/3$.

Conversely, if M/N is closer to unity, one would expect that the stagnation zones would be more prominent. $(M, N) = (3, 2)$ and $(M, N) = (2, 3)$ give $d = 2\sqrt{19/3} \simeq 5.033$ and $\theta = 66.6^\circ, 53.4^\circ, \pm 6.6^\circ$. This appears to be the case, as can be seen in Fig. 5.15. Note that in this case, d is close to an odd integer and so one would not expect to find stagnation zones in the $\theta = n\pi/3$ directions. These ‘higher-order’ stagnation zones occur instead, giving rise to two sets to stagnation zones either side of the directions along which stagnation zones are normally seen.

Finally, it is worth noting that in the more extensive plots, far from the domain there is a greater symmetry about the directions $n\pi/3 + \pi/6$. This is indicating that the lateral asymmetry of the spiral wave is becoming less important at these distances.

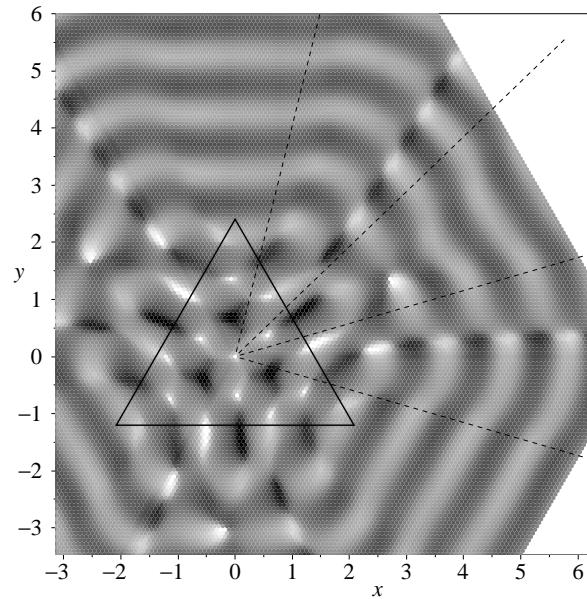


Figure 5.14: Normalized divergence plots for $d = 2\sqrt{13/3}$. The dashed lines indicate angles at which the $(M, N) = (1, 3)$ and $(M, N) = (3, 1)$ stagnation zones are predicted to lie by the PWA.

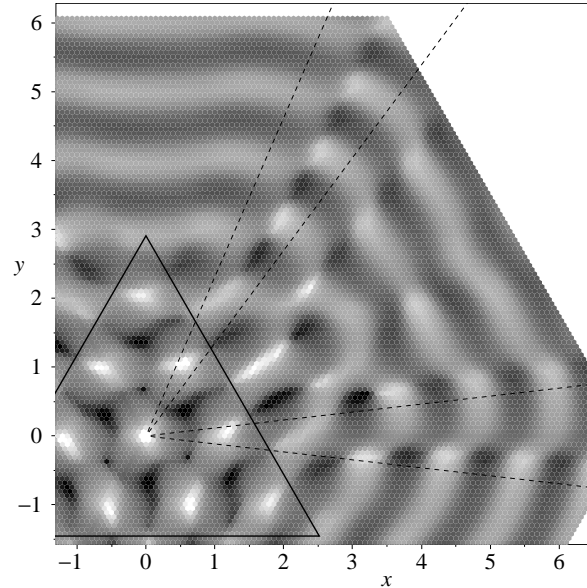


Figure 5.15: Normalized divergence plots for $d = 2\sqrt{19/3}$. The dashed lines indicate angles at which the $(M, N) = (2, 3)$ and $(M, N) = (3, 2)$ stagnation zones are predicted to lie by the PWA.

5.2 Isosceles triangular domain

The isosceles triangular domain has two parameters, length of the base, b , and the ratio, $\rho = b/h$ where h is the height. Although the isosceles triangle domain

possesses reflection symmetry about one axis, the spiral wave itself lacks this lateral symmetry. The entire vector plot must therefore be calculated.

From Figures 5.16 and 5.18 it can be seen how much the number of fixed points and the trajectory of the spiral wave tip can vary. From 5.17(a), the spiral wave core reach to the circular shape limit cycle around the domain ($\rho=1, S=1$) which is similar to the results from equilateral triangular and square domains at size of 1. Fig 5.17(b), the attractor has the triangular shape. Both of Fig 5.17(a) and (b) has one unstable focus at the centre of the domain.

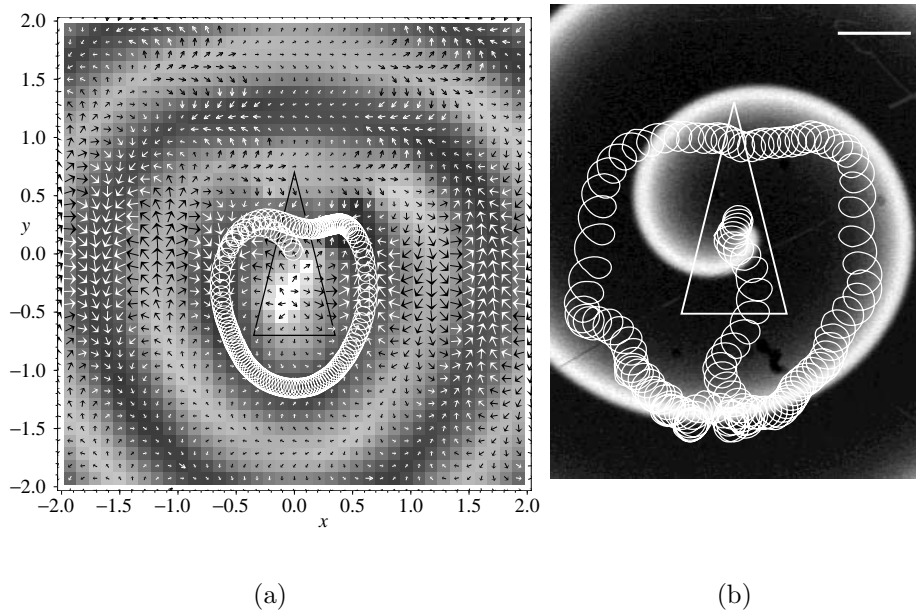


Figure 5.16: Drift velocity (a) and tip trajectory from experiment (b) for Isosceles triangular domain at $\rho=2$, $S=0.5$. Scale bar: 1 mm.

From the results, it will be seen that for a given fixed area, the domain ratio has a big influence on the shape of the trajectory. In Figure 5.16, the results show that there is one unstable focus at the centre and the spiral tip moves from the centre and goes around the domain but makes a wavy curve above the centre near the top and then repeats the path. From the vector plot, there are no other fixed points outside the domain. Only stable and unstable limit cycles are found outside the domain. In Figure 5.18(a-b), the trajectories (experimental results) did not reach the limit cycle. The tip moves to stagnation zone at the left-hand side outside the domain (Fig 5.18(a)) and the tip in (Fig 5.18(b)) moves to stable focus at the right-hand side under the

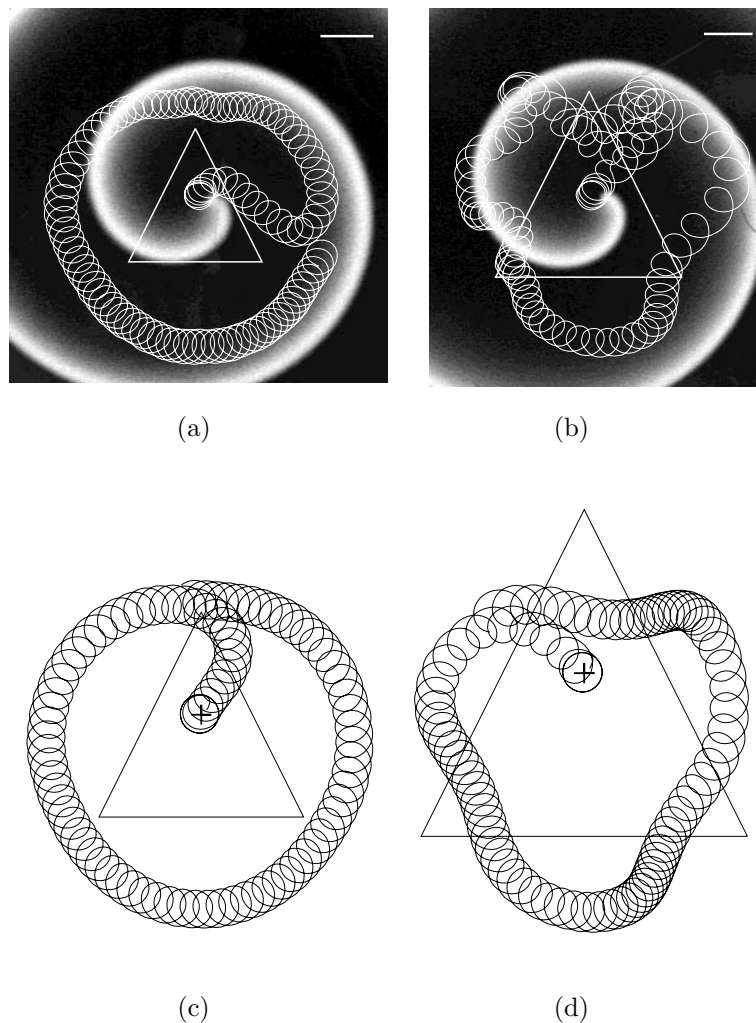


Figure 5.17: Comparison of experimental results (a,b) with simulation (c,d) of isosceles triangle domain $\rho=1$ with size S 1.0 and 1.3. Scale bar: 1 mm.

base side of the domain. There is one unstable focus at the centre, two saddle nodes, one unstable focus at the side of domain and two stable foci outside the domain (Fig 5.18(c)).

From Figure 5.19, the vector plots show how the spiral core trajectories vary with different ratios. As the ratio increases, the limit cycles get larger. For ρ in between 0.25 to 4, there are stable and unstable limit cycles around the domain and each domain has one unstable focus at the centre. The interesting point is at $\rho = 0.25$ and 4, the fixed points are found around the domain. At $\rho = 4$ Fig. 5.19(e), there are two unstable foci, two saddle nodes and one stable focus around the domain. The stable limit cycle attractor is found quite far

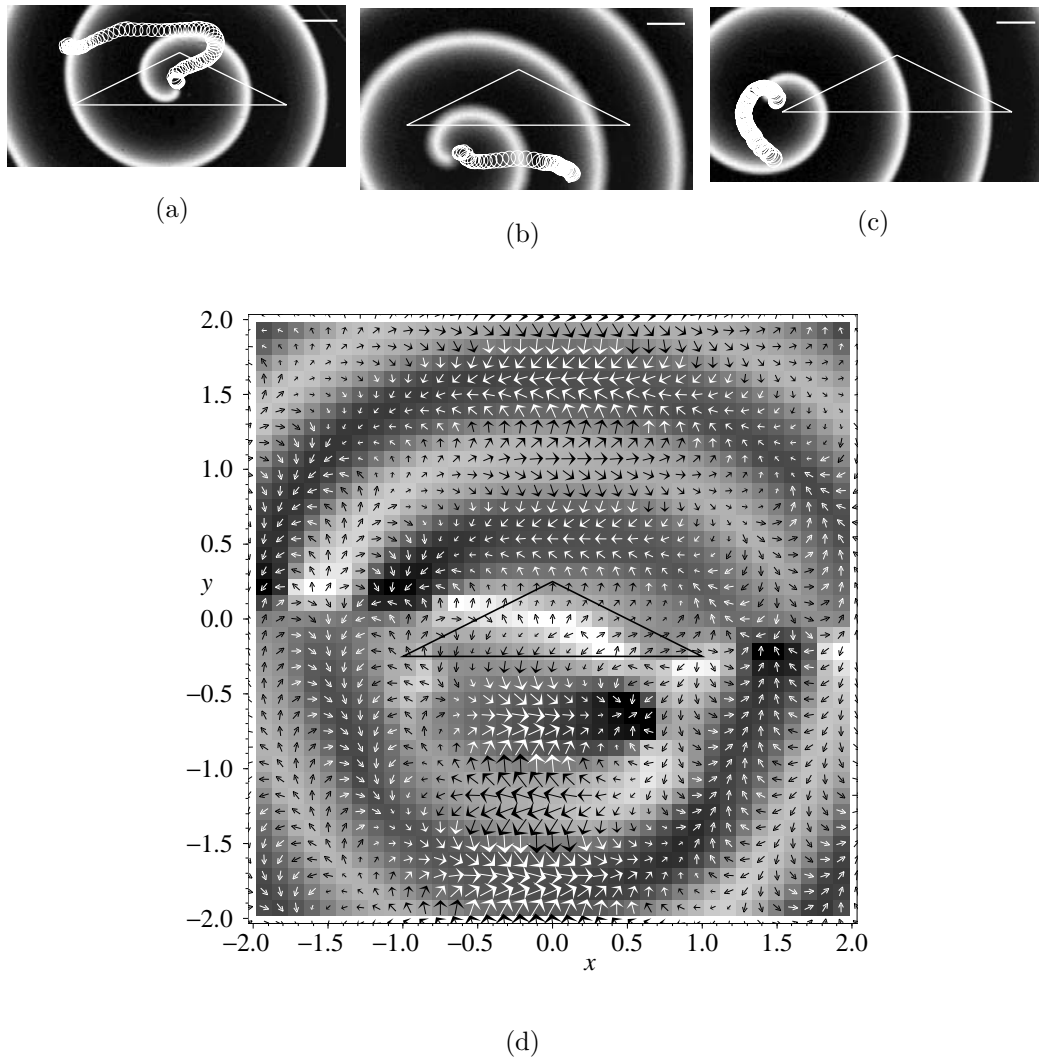
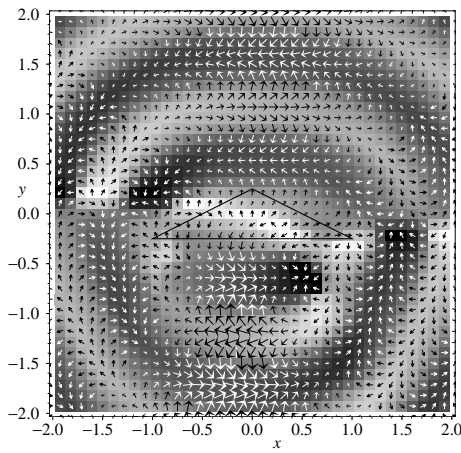


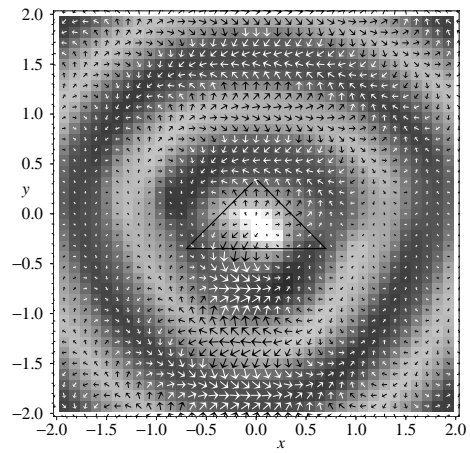
Figure 5.18: Trajectories of spiral wave tip at different starting point (a-c) and drift velocity plot (d) for isosceles triangular domain with $\rho = 0.25$, $S = 0.5$. Scale bar: 1 mm.

away from the domain. The similarity between $\rho = 0.25$ and 4 is that there are five fixed points around the domain and the limit cycles are found far away from the domain (Fig. 5.19(e) and (d), respectively).

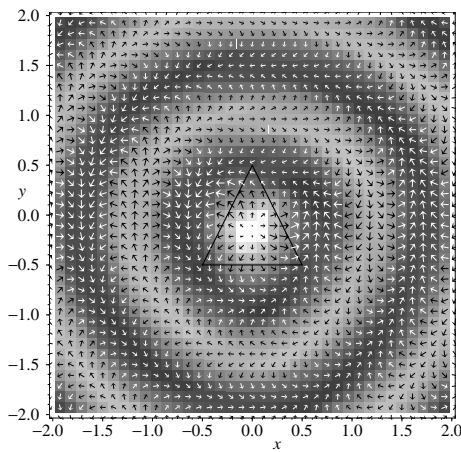
Some of the features seen in the vector plots can be analysed using the PWA. Firstly, for small ρ one would expect to see express zones above and below the triangle. These would be a result of a wavefront suddenly crossing the longest edge giving rise to a large jump in $B(t)$. Such express zones are seen in Fig. 5.18(d). Second, one would also expect to see express zones on



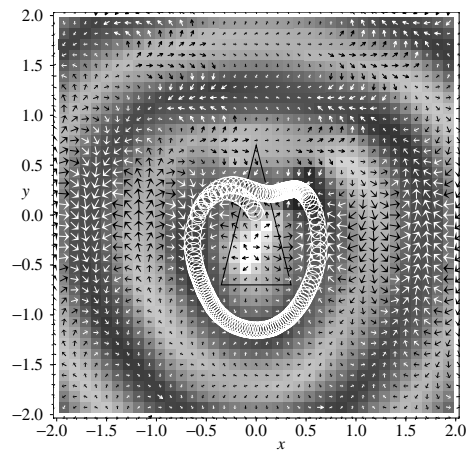
(a)



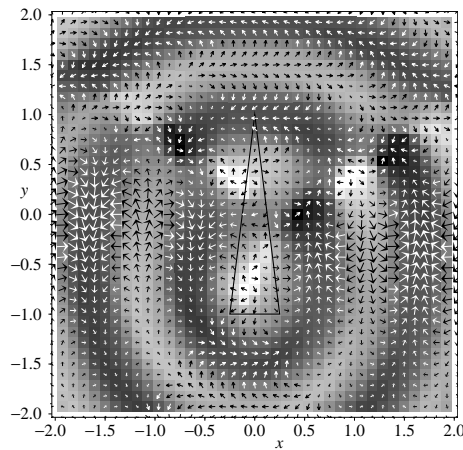
(b)



(c)



(d)



(e)

Figure 5.19: The vector plot for various ratio with Isosceles triangle size $S=0.5$, ρ is (a)-(e); 0.25, 0.5, 1, 2 and 4 respectively.

either side of the triangle when $b < 1$ and ρ is large. Wavefronts travelling in the $\theta = 0^\circ, 180^\circ$ directions will cause a sudden increase in $B(t)$ when they cross the domain. The sudden increase in $B(t)$ will result in a large first Fourier component and hence a large drift velocity (see section 3.2). Express zones of this type are apparent in Fig. 5.19(d) and (e).

Finally, stagnation zones should occur far from the domain in the directions $\theta = 0^\circ, 180^\circ$ when $b = 2n$ where n is an integer. In such cases the number of wavefronts whose length inside the domain is increasing will always be balanced by an equal number whose length inside the domain is decreasing. This type of stagnation zone is seen in Fig. 5.19(a).

5.3 Discussion

In the analysis of spiral wave dynamics under feedback control via an triangular domains, we have seen two basic types of behaviour. First, trajectories beyond some critical distance from the centroid (this distance increasing with domain size) generally will be attracted to stable limit cycles. In contrast to the results from circular and square domains, both experimental measurements and computational calculations show that these will in general be lobed if the domain is sufficiently large. The plane wave approximation tells us that these lobed limit cycles will occur at arbitrarily large distances from the centroid and that as the domain size is increased, each limit cycle will only last for a limited range of d before being destroyed. Parts of the attracting regions making up such a destroyed limit cycle some distance from the domain will later join up to form a new limit cycle. Second, inside large domains we see a regular array of stable and unstable fixed points.

Although the existence of express zones and stagnation zones is apparent in the experimental and computational results of earlier studies, this appears to be the first time they have been commented upon. In the control of a spiral wave they are of great importance. If a spiral tip is to be moved from one region to another, like stable fixed points, stagnation regions are to be avoided. Conversely, rapid movement of the spiral core could be achieved by choosing a path composed of express zones.

The stagnation zones we have reported here are not unique to feedback

via triangular domains. Using the PWA it can be seen that they would be expected to occur, for instance, aligned with the vertices of a square domain and be the most prominent when $d = \sqrt{2}n$ for integer n . Such vertex-aligned stagnation zones are evident in Fig. 2(d) of Ref. [48]. It is also straightforward to understand why the very extended stagnation zone occurs in the case of the rhombus-shaped sensory domain in Fig. 1.16(g).

The PWA approach introduced here was presented with the caveat of only applying far from the domain. Nevertheless, it is of note that some of its predictions for the drift vector field, such as the location of the express zone centres, are also reasonably accurate quite near the domain.

The experimental results show how it is possible to control the dynamics of spiral wave in the light-sensitive BZ solution. Modulation of light intensity depends on the integral of the wave activity inside a triangular sensory domain. The measured spiral wave trajectories in laboratory behave as the numerical work predicts. The experimental results also show the possibility of observing spiral wave dynamic which is some distance outside the domain.

Chapter 6

Conclusion

In this thesis we have looked at the effect of non-local feedback via triangular domains on the trajectory of the spiral core in excitable systems. In the experimental work, studies were performed on the light-sensitive BZ reaction. Numerical studies were carried out using Zykov's idealized excitable system model [46]. The experiment has shown that the movement of the spiral wave core can be controlled using the feedback mechanism with a triangular sensory domain.

In addition to obtaining specific results on how the size and shape of the domain affects the trajectories, we have introduced new ways to present data, classify, and account for the results. Plotting the drift vector arrows with colour coding on a background whose shade reflects the normalized divergence makes it much easier to see the attractors and repellors. The existence of stable and unstable fixed points in such plots is now well-known. However, regions where the motion of the spiral core is unusually fast or slow are also important. We have named these express and stagnation zones, respectively. The express zones are apparent on vector plots by the large size of the arrows compared to neighbouring regions. The stagnation zones, on the other hand, appear as particularly dark or bright regions on normalized divergence plots.

The plane wave approximation we have suggested is a simple to use tool to obtain quick results that can account for some of the features of the vector plot far from the domain. In particular, it can be used to account for the positions of express and stagnation zones far from the domain. It also indicates for what domain parameters such zones will be found and how strong they will be.

We used the PWA for the directions $\theta = n\pi/6$ since they turn out to correspond to the centres of express or stagnation zones and the expressions for $B(t)$ in these cases are the most straightforward to analyse. In addition, some further values of θ were involved when predicting directions of higher-order stagnation zones for specific values of d . Applying our PWA techniques and their extension through examining the case for other angles to explain features of drift vector fields for this and other domain geometries is an interesting topic for future investigation.

Bibliography

- [1] J D Murray. *Animal Coat Pattern and Other Practical Application*. Springer-Verlag, Berlin, 1990.
- [2] R Hoyle. *Pattern Formation: An Introduction to Method*. Cambridge University Press, UK, 2006.
- [3] T Nozakura and S Ikeuchi. Formation of dissipative structures in galaxies. *The Astrophysical Journal*, 279:40–42, 1984.
- [4] A L Hodgkin and A F Huxley. A quantitative description of membrane current and its application to conduction and excitation in nerve. *J Physiol.*, 117:500–544, 1952.
- [5] J M Davidenko, A V Pertsov, R Salomonsz, W Baxter, and J Jalife. Stationary and drifting spiral waves of excitation in isolated cardiac muscle. *Nature*, 355:349–51, 1992.
- [6] F Siegert and C J Weijer. Digital image processing of optical density wave propagation in *dictyostelium discoideum* and analysis of the effects of caffeine and ammonia. *J. Cell Sci.*, 93:325–35, 1989.
- [7] I S Nadal. http://chaos.usc.es/web_estrustruct/principal_ing.html.
- [8] A M Turing. The chemical basis of morphogenesis. *Philosophical Transactions of the Royal Society (B)*, 237:37–72, 1952.
- [9] R A Fischer. The wave of advance of advantageous genes. *Ann Eugenics*, 7:355–369, 1937.

- [10] V S Zykov. Analytical evaluation of the dependence of the speed of an excitation wave in a two-dimensional excitable medium on the curvature of its front. *Biophysics*, 25:906–911, 1980.
- [11] I R Epstein and J A Pojman. *An Introduction to Nonlinear Chemical Dynamic: Oscillations, Waves, Patterns and Chaos*. Oxford University Press, New York, 1998.
- [12] A T Winfree. Spiral waves of chemical activity. *Science*, 175:634–6, 1972.
- [13] S Jakubith, H H Rotermund, W Engel, A von Oertzen, and G Ertl. Spatiotemporal concentration patterns in a surface reaction: Propagating and standing waves, rotating spirals, and turbulence. *Phys. Rev. Lett*, 65:3013–6, 1990.
- [14] X Huang, W C Troy, Q Yang, H Ma, C R Laing, S J Schiff, and Jian-Young Wu. Spiral waves in disinhibited mammalian neocortex. *Neurosci*, 24:9897, 2004.
- [15] S C Müller, T Plesser, and B Hess. Two-dimensional spectrophotometry of spiral wave propagation in the Belousov-Zhabotinskii reaction. *Physica D*, 24:87–96, 1987.
- [16] A T Winfree. Scroll-shaped waves of chemical activity in three dimensions. *Science*, 181:937, 1973.
- [17] A T Winfree. Varieties of spiral wave behavior: an experimentalist's approach to the theory of excitable media. *Chaos*, 1:303–34, 1991.
- [18] V S Zykov. Cycloid circulation of spiral waves in an excitable medium. *Biofizika*, 31:862–5, 1986.
- [19] G Li, Q Ouyang, V Petrov, and H L Swinney. Transition from simple rotating chemical spirals to meandering and traveling spiral. *Phys. Rev. Lett*, 77:2105–8, 1996.
- [20] D Barkley. A model for fast computer simulation of waves in excitable media. *Physica D*, 49:61–70, 1991.

- [21] R Kapral and K Showalter. Spiral meandering. In P G Mezey, editor, *Chemical Waves and Patterns*, page 165. Kluwer Academic, Netherlands, 1995.
- [22] J M Starobin and C F Starmer. Common mechanism links spiral wave meandering and wave-front-obstacle separation. *Phys. Rev. E*, 55:1993–6, 1997.
- [23] Zs Nagy-Ungvarai, J Ungvarai, and S C Müller. Complexity in spiral wave dynamics. *Chaos*, 3:15, 1993.
- [24] D Barkley, M Kness, and L S Tuckerman. Spiral-wave dynamics in a simple model of excitable media: The transition from simple to compound rotation. *Phys. Rev. A*, 42:2489–92, 1990.
- [25] T Plesser, S C Müller, and B Hess. Spiral wave dynamics as a function of proton concentration in the ferriin-catalyzed Belousov-Zhabotinsky reaction. *J. Phys. Chem*, 94:7501–7, 1990.
- [26] O Steinbock, V S Zykov, and S C Müller. Control of spiral-wave dynamics in active media by periodic modulation of excitability. *Nature*, 366:322–4, 1993.
- [27] S Grill, V S Zykov, and S C Müller. Spiral wave dynamics under pulsatory modulation of excitability. *J. Phys. Chem.*, 100:19082–8, 1996.
- [28] S Kantrasiri, P Jirakanjana, and O-U Kheowan. Dynamics of rigidly rotating spirals under periodic modulation of excitability. *Chem.Phys.Lett*, 416:364–9, 2005.
- [29] R-M Mantel and D Barkley. Periodic forcing of spiral wave in excitable media. *Phys. Rev. E*, 54:4791–4802, 1996.
- [30] A Cimponeriu, C F Starmer, and A Bezerianos. A theoretical analysis of acute ischemia and infarction using ecg reconstruction on a 2-d model of myocardium. *IEEE TRANSACTIONS ON BIOMEDICAL ENGINEERING*, 48:41–54, 2001.

- [31] V N Biktashev and A V Holden. Design principles of a low-voltage cardiac defibrillator based on the effect of feed-back resonant drift. *J. Theor. Biol.*, 169:101–13, 1994.
- [32] O Steinbock, V S Zykov, and S C Müller. Wave propagation in an excitable medium along a line of a velocity jump. *Phys. Rev. E.*, 48:3295–8, 1993.
- [33] V S Zykov, O Steinbock, and S C Müller. External forcing of spiral waves. *Chaos*, 4:509–18, 1994.
- [34] E Mihaliuk, T Sakurai, F Chirila, and K Showalter. Feedback stabilization of unstable propagating waves. *Phys. Rev. E*, 65:065602, 2002.
- [35] V S Zykov, O-U Kheowan, O Rangsiman, and S C Müller. Instabilities of the resonance attractor for spiral waves in an excitable medium. *Phys. Rev. E*, 65:026206, 2002.
- [36] V S Zykov, G Bordiougov, H Brandtstädter, I Gerdes, and H Engel. Global control of spiral wave dynamics in an excitable domain of circular and elliptical shape. *Phys. Rev. E*, 92:018304, 2004.
- [37] V S Zykov and S C Müller. Spiral waves on circular and spherical domains of excitable medium. *Physica D*, 97:322–32, 1996.
- [38] V S Zykov and H Engel. Feedback-mediated control of spiral waves. *Physica D*, 199:243–63, 2004.
- [39] V S Zykov and H Engel. Dynamics of spiral waves under global feedback in excitable domains of different shapes. *Phys. Rev. E*, 70:016201, 2004.
- [40] V S Zykov and H Engel. Resonance attractors of spiral waves in excitable media under global feedback. *Phys. Rev. E*, 66:016206, 2002.
- [41] S Grill, V S Zykov, and S C Müller. Feedback-controlled dynamics of meandering spiral waves. *Phys. Review. Letter*, 75:3368–71, 1995.
- [42] O-U Kheowan. Dynamics of spiral waves under feedback control in the light-sensitive Belousov-Zhabotinsky reaction. *PhD Thesis, Faculty of Graduate Studies, Mahidol University, Bangkok*, 2000.

- [43] A Karma and V S Zykov. Structure of the resonance attractor for spiral waves in excitable media. *Phys. Rev. Lett*, 83:2453–6, 1999.
- [44] D M Goldschmidt, V S Zykov, and S C Müller. Transition to irregular dynamics of spiral waves under two-channel feedback. *Phys. Rev. Lett*, 80:5220, 1998.
- [45] V S Zykov, H Brandtstädter, G Bordiougov, and H Engel. Interference patterns in spiral wave drift induced by a two-point feedback. *Phys. Rev. E*, 72:065201(R), 2005.
- [46] V S Zykov, A S Mikhailov, and S C Müller. Controlling spiral waves in confined geometries by global feedback. *Phys. Rev. Lett*, 78:3398–401, 1997.
- [47] O-U Kheowan, V S Zykov, and S C Müller. Transition from local to global feedback control of spiral wave dynamics. *Phys. Chem. Chem. Phys.*, 4:1334–8, 2002.
- [48] O-U Kheowan, S Kantrasiri, P Wilairat, U Storb, and Stefan C Müller. Spiral wave dynamics under feedback control derived from a variety of sensory domains. *Phys. Rev. E*, 70:046221, 2004.
- [49] O-U Kheowan, S Kantrasiri, C Uthaisar, V Gáspár, and S C Müller. Spiral wave dynamics controlled by a square-shaped sensory domain. *Chem. Phys. Lett*, 389:140–4, 2004.
- [50] O-U Kheowan, C-K Chan, V S Zykov, O Rangsiman, and S C Müller. Spiral wave dynamics under feedback derived from a confined circular domain. *Phys. Rev. E*, 64:035201, 2001.
- [51] A M Zhabotinskiy. Periodic processes of the oxidation of malonic acid in solution (study of the kinetics of Belousov’s reaction). *Biofizika*, 9:306–311, 1964.
- [52] R J Field, E Körös, and R M Noyes. Oscillations in chemical systems. II. Thorough analysis of temporal oscillation in the bromate-cerium-malonic acid system. *J. Am. Chem. Soc.*, 94:8649–64, 1972.

- [53] M Jinguji, M Ishihara, and T Nakazawa. Primary process of illumination effect on the $\text{Ru}(\text{bpy})_3^{2+}$ -catalyzed Belousov-Zhabotinskii reaction. *J.Phys.Chem*, 96:4279–81, 1992.
- [54] M K Ram Reddy, Zs Nagy-Ungvarai, and S C Müller. Effect of visible light on wave propagation in the ruthenium-catalyzed Belousov-Zhabotinsky reaction. *J. Phys. Chem*, 98:12255–59, 1994.
- [55] M K Ram Reddy, Z Szlavik, Zs Nagy-Ungvarai, and S C Müller. Influence of light on the inorganic part of the ruthenium-catalyzed Belousov-Zhabotinsky reaction. *J. Phys. Chem*, 99:15081–85, 1995.
- [56] L Kuhnert and H J Krug. Kinetic of chemical waves in the acidic bromate-malonic acid- $\text{Ru}(\text{bpy})_3^{2+}$ system in comparison with the ferroin system. *J.Phys.Chem*, 91:730–33, 87.
- [57] B Neumann, Zs Nagy-Ungvarai, and S C Müller. Interaction between silica gel matrices and the Belousov-Zhabotinsky reaction. *Chem. Phys. letter*, 211:36–40, 1993.
- [58] D M Goldschmidt. Einzel- und mehrkanalrückkopplung von spirallen in der photosensitiven Belousov-Zhabotinsky-reaction. Diplomarbeit, Drittes Physikalisches Institut der Georg-August-Universität zu Göttingen, 1995.

Curriculum Vitae

Personal Details

Name: Somprasong Naknaimueang

Date of Birth: 24 May 1973

Place of Birth: Nakhonratchasima

Nationality: Thai

Educations

1978-1990: St.Mary School, Nakhonratchasima, Thailand.

1991-1994: Bachelor degree (physics), Mahidol University, Bangkok, Thailand
Senior Project *Quantum Hall Effect*.

1995-1999: Master degree (physics), Mahidol University, Bangkok, Thailand
Thesis title *Speech Analysis Using The Wavelet Transform*

1997-2000: Teacher Assistant in the physics department, Mahidol University
Bangkok Thailand

Teaching Elementary physics course for Medical student.

Teaching physics laboratory course for engineering student.

2001-2006: Otto-von-Guericke University Magdeburg .